Morphological and Star Formation Properties of Cosmic Noon Massive Quiescent Galaxies

A Thesis

submitted to

Indian Institute of Science Education and Research Pune

in partial fulfillment of the requirements for the

BS-MS Dual Degree Programme

by

Vaidik Prasal

Indian Institute of Science Education and Research Pune

Dr. Homi Bhabha Road,

Pashan, Pune 411008, INDIA.

March, 2026

Supervisor: Prof. Yogesh Wadadekar

Certificate

This is to certify that this dissertation entitled 'Morphological and Star Formation Properties of Cosmic Noon Massive Quiescent Galaxies' towards the partial fulfillment of the BS-MS dual degree programme at the Indian Institute of Science Education and Research, Pune represents study/work carried out by Vaidik Prasal at Indian Institute of Science Education and Research, Pune under the supervision of Prof. Yogesh Wadadekar, Professor-H, National Centre for Radio Astrophysics - TATA Institute of Fundamental Research (NCRA-TIFR), Pune, during the academic year 2025-26.

Vaidik Prasal

Prof. Yogesh Wadadekar

Committee:

Prof. Yogesh Wadadekar

Dr Arka Banerjee

This thesis is dedicated to my family

Declaration

I hereby declare that the matter embodied in the report entitled 'Morphological and Star Formation Properties of Cosmic Noon Massive Quiescent Galaxies' are the results of the work carried out by me at the National Centre for Radio Astrophysics - TATA Institute of Fundamental Research (NCRA-TIFR), Pune, under the supervision of Prof. Yogesh Wadadekar and the same has not been submitted elsewhere for any other degree.

Vaidik Prasal

Prof. Yogesh Wadadekar

Acknowledgments

I want to thank Prof. Yogesh Wadadekar for providing me with the opportunity to work on this project. I express my gratitude for his guidance, support, and encouragement throughout the course of this research. This work was also made possible by the computational resources provided by the National Centre for Radio Astrophysics (NCRA). I would also like to thank Mr. Pralay Biswas and Ms. Rashi Jain for their guidance, insights, and for providing me with the catalog data. I am grateful to Dr Vivek Kumar Jha for the fruitful discussions and suggestions. I also thank Dr. Arka Banerjee for his valuable feedback and suggestions on the thesis. Finally, I would like to thank my family and friends, Subhankar, Saptarshi, Yash, Tushar, and Tanmaay, for their support and encouragement throughout my academic journey.

This work is currently submitted to the Astrophysical Journal (ApJ) and can be found at `https://doi.org/10.48550/arXiv.2605.02493`.

Contributions

The research presented in this thesis was conducted by Vaidik Prasal under the supervision of Prof. Yogesh Wadadekar. All scientific analysis, interpretation of results, and writing of the thesis are the original work of the author. The `BAGPIPES` catalog used in this study was provided by Mr. Pralay Biswas and Ms. Rashi Jain.

Generative AI Usage

Generative AI tools were used in the preparation of this thesis in accordance with the 'Guidelines for Generative AI usage at IISER Pune'. The specific usage is detailed below:

1. **Wrapper code for Python packages:** Generative AI (various models in Github Copilot) was used to generate wrapper code for running Python packages including `PySersic` , `statmorph` , `BAGPIPES` , and `piXedfit` . The AI-generated code was reviewed, tested, and modified by the author to ensure correctness and compatibility with the analysis pipeline.

2. **LaTeX table generation:** Generative AI (various models in Github Copilot) was used to write code for converting data outputs into LaTeX-formatted tables. The generated code was verified and adapted by the author to match the formatting requirements of the thesis.

3. **Plotting code:** Generative AI (various models in Github Copilot) was used to generate code for creating plots used in the analysis. The plotting scripts were reviewed, tested, and modified by the author to ensure accuracy and appropriate visualization of the scientific results.

All AI-generated code was critically reviewed, tested, and modified as necessary before use. The scientific conclusions and interpretations presented in this thesis are entirely the author's own work. The relevant code files contain comments attributing AI assistance as per the guidelines.

Abstract

We analyze the star formation and morphological properties of massive quiescent galaxies at cosmic noon ($2 < z < 3$) in the Abell 2744 field, using deep JWST NIRCam broadband and medium-band imaging from the UNCOVER Treasury program and the MegaScience survey, complemented by archival HST data. Using `BAGPIPES` SED modeling, we select 14 unique massive quiescent galaxies ($M_* \gtrsim 10^{10}$ $M_\odot$, sSFR $< 0.2/t_{\rm age}$). Morphological analysis with `statmorph` and `PySersic` reveals that most galaxies are intermediate type or S0s with a median Sérsic index $n \sim 4$, consistent with bulge-dominated systems. This value remains constant over $z \sim 1.5$–4, indicating that the morphology of massive galaxies is linked to their quiescence since at least $z \sim 4$. Spatially resolved SED modeling with `piXedfit` shows that $\sim 79\%$ of galaxies exhibit positive radial sSFR gradients, providing direct evidence for inside-out quenching, with the mean sSFR increasing by ~ 2 dex from $R/R_e = 0.5$ to 4.5. Formation time (t_{50}) profiles confirm that inner regions formed ≈ 0.5 Gyr earlier, on average, than the outer regions, and quenching timescale profiles show that the cores were quenched more rapidly than the outskirts. Some galaxies show weak indications of possible AGN activity. Most galaxies are compact, with a mean half-mass radius of $R_e = 1.95 \pm 0.13$ kpc. The observed inside-out quenching pattern and possible AGN signatures are consistent with AGN feedback playing a role in star formation cessation, while the bulge-dominated morphologies suggest morphological quenching may also contribute.

Contents

Abstract **xiii**

List of Figures **xvii**

List of Tables **xxi**

1 Introduction **1**

2 Dataset **7**

2.1 UNCOVER Survey 7

2.2 Medium Bands, Mega Science Survey 7

2.3 UNCOVER SUPER Catalog (DR3) 8

2.4 DAWN JWST Archive 8

3 Methods **11**

3.1 Sample selection using BAGPIPES 11

3.2 Stellar Population Synthesis with BAGPIPES 11

3.3 Sample selection using BAGPIPES results 12

3.4 Morphological analysis using statmorph and pysersic 14

3.5 Spatially Resolved Analysis using piXedfit 17

3.5.1 Creating an image datacube 17

3.5.2 Pixel Binning 18

3.5.3 SED modeling 19

4 Results **21**

4.1 Morphological Analysis 21

4.2 piXedfit Analysis 27

4.3 Radial Profiles 28

5 Discussion **35**

6 Summary & Conclusions **41**

A Statmorph and pysersic results for the 14 galaxies in our sample **45**

B The three lensed galaxies (Source 67) **51**

List of Figures

3.1 Our sample of 17 massive quiescent galaxies is shown here as $4'' \times 4''$ RGB images with filters F200W, F150W, and F115W, centered on the galaxies. Three of these galaxies (ID_DR3 = 45356, 45357, 45378) are multiply-lensed images of the same source, and two of them (ID_DR3 = 45370, 45398) are multiply-lensed images of another source [1]. The white circle at the bottom left represents the PSF size of the F444W filter image (FWHM = $0.''176$). This is $\approx 21\%$ higher than the empirical PSF [2]. UNCOVER uses pixel scales of $0.02''$ and $0.04''$ for short wavelength (SW) and long wavelength (LW) filters, respectively. We have also circled the foreground galaxies near galaxy ID_DR3 = 20697 and near galaxy ID_DR3 = 45378. See the text for details. 13

3.2 The stellar mass vs sSFR (in log scale, top panel) and UVJ diagram (bottom panel) for our sample of 17 massive quiescent galaxies out of all the galaxies in the survey with redshifts between 2 and 3. The quiescent selection boundary from Williams et al. [3] is shown in the UVJ plot, as a light-blue shaded region. The stellar mass vs sSFR plot shows that our sample galaxies lie well below the star-forming galaxies, consistent with their quiescent nature. The three multiply-lensed images of the first source (ID_DR3 = 45356, 45357, 45378) are marked with blue stars, and the two multiply-lensed images of the second source (ID_DR3 = 45370, 45398) are marked with green stars. The gray points represent high-redshift galaxies in the redshift range $2 < z < 4$ in the UNCOVER survey. 15

4.1 Non-parametric morphological parameters for our sample of 14 unique massive quiescent galaxies for the F200W NIRCam filter. Top: Concentration (C) vs. $\log_{10}(A)$ (asymmetry). The merger line was taken from Conselice [4], and the disk/intermediate and intermediate/elliptical boundaries were implemented following Bershady et al. [5]. Bottom: Gini coefficient vs. M_{20}. The boundary lines were implemented following Lotz et al. [6]. 22

4.2 Two-component `PySersic` fits for the galaxies in our sample in the F200W filter ($4''$ cutouts). The panels display the original images, the median models, and the resulting residual maps. The color scale limits (vmin and vmax) for the residual plots are set to ± 0.1 (in 10 nJy), where blue regions indicate less flux than the model and red regions indicate excess flux. The average absolute residual is $4.16\% \pm 1.39\%$, with values ranging from 0.38% to 22.09%. The standard deviation of the mean is calculated via bootstrapping for 1000 iterations. 24

4.3 Two-component `PySersic` fits for the galaxies in our sample in the F444W filter ($4''$ cutouts). The panels display the original images, the best-fit models, and the resulting residual maps. The color scale limits (vmin and vmax) for the residual plots are set to ± 0.1 (in 10 nJy), where blue regions indicate less flux than the model and red regions indicate excess flux. The average absolute residual is $1.48\% \pm 0.67\%$, with values ranging from 0.16% to 10.25%. The standard deviation of the mean is calculated via bootstrapping for 1000 iterations. 25

4.4 Top: This is an RGB image (using F444W, F356W, and F277W) of galaxy `ID_DR3` = 14207, which is likely to have undergone tidal disruptions due to interactions with `ID_DR3` = 14206, distinctly visible in the long wavelength filters. Bottom: This is an RGB image (using F200W, F150W, and F115W) of galaxy `ID_DR3` = 18351, which is likely to be a merger candidate. We can see nearby objects to its left with very similar redshifts. Both the cutouts are of $8''$. Surrounding galaxies with similar redshifts (obtained using `BAGPIPES`, within the error bars of their photometric redshifts) are marked in the cutouts. 26

4.5 Figures (a), (e), and (i) are the RGB images (using F115W, F150W, and F200W filters), (b), (f), and (j) are the bin index maps, (c), (g), and (k) are the pixel-level stellar mass maps, and (d), (h), and (l) are the pixel-level SFR maps for the three interacting galaxies in our sample (`ID_DR3` = 14207, 14897, and 18351). The spectra of different bins for these three galaxies are shown in the figures on the right. Filled circles are the model fluxes, and the open squares are the observed fluxes, with error bars. The solid lines are the best-fit SEDs for each bin. 29

4.6 Mean radial profiles for the stellar mass, SFR, and sSFR for our sample of 14 galaxies. The top panels show the profiles normalized by the half mass radius (R_e), following Laishram et al. [7]. The bottom panels show the profiles with the radius R in increments of 0.3 kpc for direct comparison with Haryana et al. [8]. Left: Stellar mass radial profiles. Middle: SFR radial profiles. Right: sSFR radial profiles. The red dashed line in the stellar mass radial profile plot in the bottom panel is the PSF profile for the F444W filter, which is the reference filter for the PSF matching. We can observe the increasing sSFR gradient, which indicates inside-out quenching. The error bars are the 68% confidence intervals of the mean, derived from bootstrapping for 1000 iterations. 30

4.7 Mean radial profiles of the $U-V$ and $V-J$ colors as a function of radius in kpc for our sample of 14 galaxies. The error bars are the 68% confidence intervals of the mean, derived from bootstrapping for 1000 iterations. The profiles are derived from the `piXedfit` SED modeling. 31

4.8 Mean radial profiles of the formation time ($t_{50,\mathrm{piX}}$, on the left) and the quenching timescale ($t_{q,\mathrm{piX}} - t_{50,\mathrm{piX}}$, on the right) for our sample of 14 galaxies. The top panels show the profile normalized by the half mass radius (R_e) in bins of 0.5 R_e, while the bottom panels show the profile with radius in kpc in bins of 1 kpc. The error bars are the 68% confidence intervals of the mean, derived from bootstrapping for 1000 iterations. The positive gradient of the formation time profile indicates that the inner regions (< 4 kpc) of the galaxies formed earlier than the outer regions (> 4 kpc) by ≈ 0.5 Gyr, whereas the quenching timescale profile implies that the cores were quenched faster than the outer regions. 32

4.9 Star formation histories (SFHs) for all galaxies in our sample from BAGPIPES SED modeling. Each panel shows the posterior SFH for one galaxy, with the blue vertical line indicating the formation time ($t_{50,\mathrm{BG}}$) and the red vertical line indicating the quenching time ($t_{q,\mathrm{BG}}$). The SFHs indicate rapid early mass assembly followed by quenching in ≈ 1.4 Gyr. 33

5.1 Morphological parameters as a function of redshift for our sample of massive quiescent galaxies (F277W, blue filled stars) compared with literature values. Top panels: Sérsic index (n) comparison. Bottom panels: Axis ratio (q) comparison. Comparison samples include UVJ-selected quiescent galaxies from van der Wel et al. [9, $\log(M_*/M_\odot) > 10$], Straatman et al. [10, $10.6 < \log(M_*/M_\odot) < 11.25$], and Ito et al. [11, $9.8 < \log(M_*/M_\odot) < 11.4$]; photometrically selected galaxies from Marsan et al. [12, $\log(M_*/M_\odot) > 11.25$]; and sSFR-selected quiescent galaxies from Martorano et al. [13, $\log(M_*/M_\odot) > 10$] (F277W morphology cross-matched with COSMOS2020 catalog; Weaver et al. 14). Individual spectroscopically confirmed massive quiescent galaxies are also shown: SXDS-27434 [15, 16, 11, $\log(M_*/M_\odot) = 11.06$], GS-9209 [17, $\log(M_*/M_\odot) = 10.58$], RUBIES-EGS-QG-1 [18, $\log(M_*/M_\odot) = 10.9$], and galaxies from Esdaile et al. [19, $11 < \log(M_*/M_\odot) < 11.3$], Lustig et al. [20, $10.8 < \log(M_*/M_\odot) < 11.3$] and Kawinwanichakij et al. [21, $10.2 < \log(M_*/M_\odot) < 11.2$]. On the right panels, the median Sérsic indices (top) and median axis ratios (bottom) for our sample are shown as blue-filled stars (F277W), brown-outlined stars (F444W), and green-filled stars (F200W). All the median error bars are the 68% confidence intervals derived from bootstrapping for 1000 iterations. 39

B.1 BAGPIPES posterior corner plots for the three lensed images of the same galaxy: ID_DR3 = 45356 (left), 45357 (center), and 45378 (right). The bimodal posteriors in metallicity and dust (A_V) are clearly visible. 51

List of Tables

1.1 BAGPIPES fitting parameters 5

3.1 Physical properties of final sample galaxies from BAGPIPES SED fitting 14
3.2 `piXedfit` Modeling Parameters 20

5.1 Median Sérsic Index, Axis Ratio, and Bulge-to-Total Ratio Across Filters 38

A.1 Morphological parameters from statmorph analysis across multiple filters 45
A.2 Pysersic fit results across multiple filters 47

Chapter 1

Introduction

Massive quiescent galaxies at high redshifts ($z > 2$) challenge our understanding of galaxy evolution and serve as critical laboratories for testing galaxy formation and evolution models [22, 23]. These systems are unusual because they have built up a large stellar mass and have thereafter stopped forming stars by the time the Universe was about 3 billion years old, a period when star formation was generally highly active [24]. Understanding how, when, and why these galaxies quenched remains one of the central open questions in extragalactic astronomy. The existence of massive quiescent galaxies at high redshifts poses a problem for many theoretical models of galaxy formation because they require extremely rapid formation and quenching mechanisms to assemble large stellar masses (often $> 10^{11}$ $M_{\odot}$) and then to completely reverse the star-formation process, all within the first few billion years after the Big Bang.

Cosmological hydrodynamical simulations such as IllustrisTNG [25], EAGLE [26], SIMBA [27], and FLAMINGO [28] make predictions about the number densities of massive quiescent galaxies that can be compared with observations. Recent observations with the James Webb Space Telescope (JWST) have found number densities of massive quiescent galaxies at $z > 3$ that exceed predictions from even the most recent semi-analytic and hydrodynamic models [29, 30, 31]. This tension between simulations and observations suggests that models may underestimate the efficiency of early mass assembly and quenching processes, or that the prescriptions for star formation and feedback at early times require revision [18].

To address these tensions and explain the rapid shutdown of star formation, several physical mechanisms have been proposed. Active galactic nucleus (AGN) feedback is widely considered

the leading candidate for quenching massive galaxies, operating in both "quasar mode" (radiatively driven winds) and "jet/radio mode" (mechanical energy injection) [32, 33, 34]. Recent JWST observations of mass outflows from cosmic noon massive quiescent galaxies provide direct evidence for AGN-driven feedback as a quenching mechanism [35, 36, 37]. A complementary mechanism is morphological quenching, where the growth of a massive stellar bulge stabilizes the gas disk against fragmentation and collapse, effectively shutting down star formation even when cold gas is present [38].

The physical mechanisms driving this rapid quenching are closely tied to the structural evolution of these galaxies. A defining feature of massive quiescent galaxies at $z > 2$ (extending to $z \sim 4$) is their extreme compactness, which is most accurately revealed in the rest-frame near-infrared where stellar mass distributions, dominated by low mass stars, are more clearly traced [13, 8]. These systems exhibit typical effective radii of $R_e \sim 0.6$–1.5 kpc, a factor of 4 to 6 smaller than local ellipticals of comparable mass, resulting in stellar mass surface densities approximately two orders of magnitude higher than their low-redshift counterparts [39, 13, 8].

A recent spatially resolved analysis [8] indicates that while their central 1 kpc cores were already as dense as local quiescent galaxies by $z \sim 4$, their subsequent size evolution is driven by a two-phase assembly process: initial growth dominated by major mergers at $z \gtrsim 2$, followed by minor dry mergers at $z \lesssim 2$ that primarily build up the galaxy outskirts while leaving the dense core intact. Cosmological simulations also support this size evolution driven primarily by minor mergers [40, 41, 42, 43].

Consistent with their compact sizes and centrally concentrated mass distributions, massive quiescent galaxies at $z > 2$ typically exhibit high Sérsic indices ($n \sim 3$–6), indicating concentrated, bulge-dominated light profiles similar to local elliptical galaxies [44, 9, 45]. This suggests that the central bulge component was already in place by $z \sim 2$–3, with galaxies subsequently growing their envelopes through dry merging.

An alternate way for quantifying galaxy morphologies, particularly for high-redshift galaxies with small angular size, is by using non-parametric measures such as the CAS (Concentration–Asymmetry–Smoothness) system [46, 4] and the Gini–M_{20} plane [47, 6]. Quiescent galaxies at $z > 2$ tend to occupy the high-concentration, low-asymmetry region of the CAS parameter space [4, 48, 49], consistent with smooth, symmetric morphologies [5, 48, 50]. In the Gini–M_{20} plane, they

fall in the "bulge-dominated (E/S0)" region [6, 48]. While these global morphological measures reveal the overall structural properties of quiescent galaxies, understanding the spatial distribution of their stellar populations requires spatially resolved analyses.

Spatially resolved studies of massive quiescent galaxies provide critical constraints on how star formation shuts down within individual systems. The paradigm of inside-out quenching, where star formation is first suppressed in the central regions while the outskirts remain active, has emerged from theoretical predictions and observational evidence spanning from the local universe to high redshifts.

Observations of massive galaxies at $z \sim 2.2$ reveal the inside-out quenching process, where star formation ceases in the dense inner regions on timescales of $\lesssim 1$ Gyr while outer disks remain active, rapidly building central mass densities comparable to local early-type galaxies [51]. This is supported by high-resolution molecular gas imaging at $z \sim 2$, which shows centrally suppressed gas fractions and short depletion times in the inner 1–2 kpc [52]. Similar trends persist in the local universe; integral field surveys like the Calar Alto Legacy Integral Field Area (CALIFA) survey and the Mapping Nearby Galaxies at Apache Point Observatory (MaNGA) survey confirm that massive galaxies preferentially exhibit outwardly increasing sSFR profiles, with central bulges quenching significantly faster than their disks [53, 54]. Furthermore, Lin et al. [54] found a strong link between dense, quenched cores and bulge-dominated structures (high Sérsic indices) across all environments, demonstrating that central bulge growth plays a key role in shutting down star formation. Theoretically, cosmological simulations such as IllustrisTNG predict this inside-out quenching pattern as a natural consequence of low-accretion kinetic AGN feedback. In this framework, central kinetic winds evacuate gas from the galactic core, creating positive sSFR radial gradients that are quantitatively consistent with observations up to $z \sim 1$ [55]. Together, these studies suggest that a combination of central bulge growth and AGN-driven winds drives the rapid central quenching of massive galaxies across cosmic time.

With JWST, spatially resolved spectral energy distribution (SED) modeling [see 56, 57, for a review on SED modeling] has become possible at $z > 2$ due to JWST's unprecedented sensitivity and resolution in the near-infrared, enabling pixel-level stellar population analysis. At this redshift, the near-infrared observations have an additional advantage; they give us access to the rest-frame optical wavelengths. Recent studies have demonstrated that the majority of massive quiescent

galaxies at $z \sim 2$–3 show positive sSFR gradients, lower sSFR in the center, and higher sSFR in the outskirts, directly confirming inside-out quenching [8, 7].

In this paper, we present a comprehensive analysis of the morphological and star formation properties of massive quiescent galaxies ($M_* \gtrsim 10^{10}$ $M_\odot$) at cosmic noon ($2 < z < 3$), leveraging deep JWST NIRCam imaging from the Ultradeep NIRSpec and NIRCam ObserVations before the Epoch of Reionization (UNCOVER) Treasury program [58] and the "Medium Bands, Mega Science" [59, MegaScience] medium-band survey of the Abell 2744 lensing cluster field. We select quiescent galaxies using the Bayesian Analysis of Galaxies for Physical Inference and Parameter EStimation [60, `BAGPIPES`] code for the SED modeling of the combined HST + JWST photometry with an sSFR criterion, perform morphological analysis using `statmorph` [61, non-parametric CAS, Gini, M_{20}] and `PySersic` [62, two-component bulge and disk decomposition] across all NIRCam broadband filters, and probe the spatial distribution of stellar populations through spatially resolved SED modeling with `piXedfit` [63]. We derive pixel-level maps and radial profiles of stellar mass, star formation rate (SFR), sSFR, formation time (t_{50}), quenching timescale ($t_q - t_{50}$), and the rest-frame U$-$V and V$-$J colors to constrain the quenching history.

A key strength of our SED modeling lies in the combination of broadband and medium-band photometry. The inclusion of medium bands provides tighter constraints on photometric redshifts [59] and mitigates the systematic biases in stellar mass and SFR estimates that frequently affect broadband-only analyses [64].

This paper is organized as follows. Section 2 describes the UNCOVER and MegaScience datasets. Section 3 details our sample selection, morphological analysis, and spatially resolved SED modeling methodology. Section 4 presents the morphological properties, `piXedfit` results, and radial profiles. Section 5 discusses the implications of our findings in the context of inside-out quenching and galaxy evolution at cosmic noon. Section 6 summarizes our main conclusions. We have used the `Planck2018` cosmology [65, $H_0 = 67.66$ km s^{-1} Mpc^{-1}, $\Omega_m = 0.31$, $\Omega_\Lambda = 0.69$] throughout this work.

Table 1.1: BAGPIPES fitting parameters

Parameter	Value / Range	Description
Star Formation History (Delayed Tau Model)		
age	[0.1, 15]	Time since star formation began in Gyr
tau	[0.3, 10]	e-folding timescale of SFH decay in Gyr
massformed	[4, 15]	Log of total stellar mass formed wrt solar mass
metallicity	[0.1, 2.5]	Log of stellar metallicity wrt solar metallicity
Dust Attenuation		
type	“Calzetti"	Dust attenuation law
eta	2	Multiplicative factor for the Calzetti law
A_V	[0, 6]	V-band attenuation in mag
Nebular Emission		
logU	-3	Log of the ionization parameter
Fit Instructions		
redshift	[0, 15]	Redshift range for the fit

Chapter 2

Dataset

We utilize image mosaics, weight maps, and photometric products from the coordinated JWST surveys of the massive lensing cluster Abell 2744 ($z = 0.308$). This dataset is primarily composed of observations from the UNCOVER JWST Cycle 1 Treasury program [PIs Labbé & Bezanson; GO-2561; 58] and the MegaScience JWST Cycle 2 program [PI Suess; GO-4111; 59].

2.1 UNCOVER Survey

The primary UNCOVER NIRCam mosaic was imaged through six broadband filters (F115W, F150W, F200W, F277W, F356W, and F444W) and one medium-band filter (F410M), achieving imaging depths of $\sim$ 29–30 AB [58]. UNCOVER also obtained ultradeep NIRSpec/PRISM spectroscopy ($R \sim$ 30–300) spanning 0.6–5.3 μm for approximately 500 unique galaxies. These spectroscopic observations utilized a multi-mask strategy with total integration times ranging from 2.7 to 17.4 hours to reach continuum depths of $\sim$ 29 AB [66].

2.2 Medium Bands, Mega Science Survey

To complement the broadband imaging, we incorporate data from the MegaScience survey, which provides comprehensive medium-band coverage of the same field [59]. MegaScience delivered 29.2 arcmin^2 of deep NIRCam imaging (up to $\sim$ 30 AB) through 11 additional medium-band filters (F140M, F162M, F182M, F210M, F250M, F300M, F335M, F360M, F430M, F460M, and

F480M) and two short-wavelength broadband filters (F070W and F090W). When combined with UNCOVER, this results in a unique dataset featuring complete coverage in all 20 NIRCam broadband and medium-band filters. The inclusion of medium-band photometry reduces photometric redshift scatter ($\sigma_{\rm NMAD}$) and catastrophic outlier rates by factors of 2–3 compared to broadband-only measurements [59].

2.3 UNCOVER SUPER Catalog (DR3)

We utilize the value-added UNCOVER SUPER Catalog from the Data Release 3[1] (DR3), which provides multi-wavelength photometry for 74,020 sources in the Abell 2744 field [67, 59]. The UNCOVER team constructed this catalog using a 56.2 arcmin^2 detection image, created from a noise-weighted stack of long-wavelength filters (F277W, F356W, and F444W). The co-added mosaics incorporate data from several other public JWST programs in the Abell 2744 field, including GLASS-ERS [68], DDT-2756 (PI Chen), ALT [69], MAGNIF (PI Sun), and GO-3538 (PI Iani). The catalog also integrates archival Hubble Space Telescope imaging from the Hubble Frontier Fields (HFF) and BUFFALO programs, spanning seven filters (F435W, F606W, F814W, F105W, F125W, F140W, and F160W).

To ensure accurate SED modeling, the UNCOVER team matched all images to the F444W point-spread function (PSF) using convolution kernels. Finally, the strong lensing magnifications for all galaxies in the catalog are based on the updated mass models of Furtak et al. [1] and Price et al. [66] (taken from the DR4[2]), which utilize the deep JWST imaging to provide significantly improved constraints.

2.4 DAWN JWST Archive

The DAWN JWST Archive[3] (DJA) hosts publicly released JWST galaxy data reduced with the `grizli` [70, 71] and `msaexp` [72] reduction pipelines. We have accessed the catalog of the galaxies with grade 3 NIRSpec data from the DJA [72, 73, 74]. A grade 3 spectrum implies a robust

[1] `https://jwst-uncover.github.io/DR3.html`
[2] `https://jwst-uncover.github.io/DR4.html`
[3] `https://dawn-cph.github.io/dja/index.html`

redshift from one or more emission or absorption features. Out of the 37,528 grade 3 spectra available (as on 29th December 2025), 5 are common with our sample. For these objects, we use the spectroscopic redshifts for SED modeling, as elaborated in the next section.

Chapter 3

Methods

3.1 Sample selection using BAGPIPES

3.2 Stellar Population Synthesis with BAGPIPES

To determine the physical properties of galaxies, such as stellar mass, star formation rate, and photometric redshift, we use SED modeling. By comparing the observed photometry in various filters to synthetic spectra produced by stellar population synthesis models, we can derive joint posterior distributions for these critical parameters, which, in turn, form the basis of our quiescent galaxy sample selection.

We perform SED modeling using data from the JWST NIRCam filters (broadband and medium bands), HST/WFC3 filters (F105W, F125W, F140W, F160W), and HST/ACS filters (F435W, F606W, F814W), where available, using the `BAGPIPES` framework [60]. `BAGPIPES` provides a flexible framework for generating synthetic galaxy spectra from user-specified parameters and for fitting those models to observational data. The framework incorporates BC03 SPS models from the 2016 update of Bruzual and Charlot [75], combined with the Kroupa and Boily [76] initial mass function. Users specify prior distributions and permissible ranges for physical parameters, along with parametric forms for star formation histories. `BAGPIPES` employs the PyMultiNest nested sampling algorithm [77, 78, 79, 80] to efficiently sample the parameter space and generate model SEDs. By extensively sampling the posterior distribution, `BAGPIPES` simultaneously constrains

the photometric redshift and SPS parameters, and returns joint posterior estimates of redshift, stellar mass, star formation rate, gas-phase metallicity, and dust attenuation. We use the Nov 2022 JWST filter curves from `sedpy` [81] for our analysis. For each galaxy, we mask the filters with Signal-to-Noise Ratio (SNR) $\leqslant 3$. We also divide the fluxes by their strong lensing magnifications (μ, taken from the catalog) to correct for strong lensing. For the galaxies having a spectroscopic redshift (from DJA), we fix their redshifts to the spectroscopic value and then run `BAGPIPES` on them. See Table 1.1 for the parameters and priors used for the `BAGPIPES` modeling.

3.3 Sample selection using BAGPIPES results

Having derived the physical properties of the galaxies in the UNCOVER catalog using `BAGPIPES`, we then identify massive galaxies at cosmic noon that have already ceased significant star formation from the output catalog as follows:

- Stellar Mass: We select galaxies with stellar masses (50th percentile) $M_* \gtrsim 10^{10}\,\mathrm{M}_\odot$ to focus on the most massive systems.
- sSFR: We classify galaxies with
$$\mathrm{sSFR} < \frac{0.2}{t_{\mathrm{age}}}, \tag{3.1}$$
where t_{age} is the age of the universe at the galaxy's redshift, as quiescent, indicating minimal ongoing star formation [82, 83, 84, 29, 31].
- Redshift Range: We restrict our sample to galaxies within the redshift range $2 < z < 3$ to target the epoch of interest for cosmic noon studies.

After applying this selection, we identify a sample of 17 massive quiescent galaxies for further analysis, shown in Figure 3.1. Figure 3.2 shows the stellar mass vs sSFR plot and UVJ diagram for our sample. Among these, Furtak et al. [1] identify 3 (`ID_DR3` = 45356, 45357, 45378) as the multiply-imaged source with ID 67, and 2 (`ID_DR3` = 45370, 45398) as the multiply-imaged source with ID 69. So effectively, we have 14 unique massive quiescent galaxies in our sample. We use the least magnified image (`ID_DR3` = 45378) of the lensed source ID 67 in our analysis since the lensing has highly sheared and distorted the other two images [85]. Similarly, we use

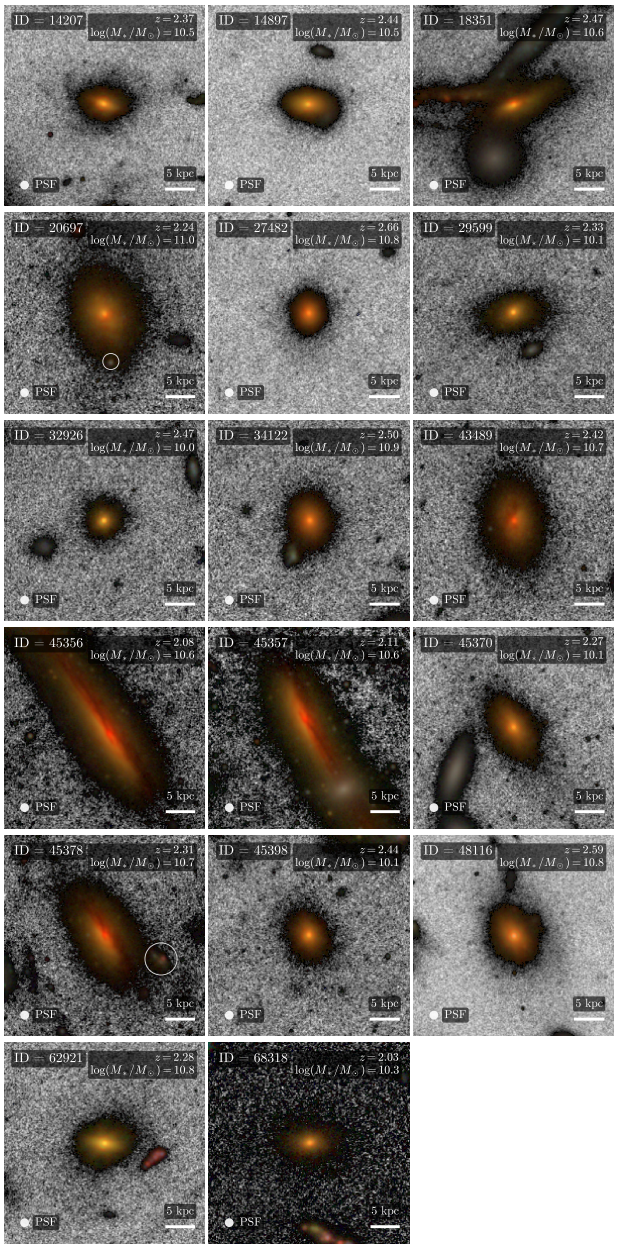

Figure 3.1: Our sample of 17 massive quiescent galaxies is shown here as $4'' \times 4''$ RGB images with filters F200W, F150W, and F115W, centered on the galaxies. Three of these galaxies (ID_DR3 = 45356, 45357, 45378) are multiply-lensed images of the same source, and two of them (ID_DR3 = 45370, 45398) are multiply-lensed images of another source [1]. The white circle at the bottom left represents the PSF size of the F444W filter image (FWHM = $0.''176$). This is $\approx 21\%$ higher than the empirical PSF [2]. UNCOVER uses pixel scales of $0.02''$ and $0.04''$ for short wavelength (SW) and long wavelength (LW) filters, respectively. We have also circled the foreground galaxies near galaxy ID_DR3 = 20697 and near galaxy ID_DR3 = 45378. See the text for details.

the less magnified image (ID_DR3 = 45398) of the lensed source ID 69 in our analysis. We note that the galaxies with the source ID 67 lie just outside or a little bit outside of the quiescent region defined by Williams et al. [3], see Figure 3.2. Nevertheless, we classify them as quiescent due to their extremely low sSFR, as can be seen in the mass–sSFR plot. Table 3.1 presents the estimated SPS parameters of the final sample.

Table 3.1: Physical properties of final sample galaxies from BAGPIPES SED fitting

ID	Age (Gyr)	$\log(M_{\rm formed}/M_\odot)$	Metallicity	τ (Gyr)	A_V (mag)	Redshift	$\log(M_*/M_\odot)$	SFR ($M_\odot$/yr)	$\log(\mathrm{sSFR/yr^{-1}})$	MW age (Gyr)	μ
14207	$2.55^{+0.14}_{-0.17}$	$10.79^{+0.02}_{-0.02}$	$0.258^{+0.164}_{-0.074}$	$0.32^{+0.03}_{-0.01}$	$0.47^{+0.12}_{-0.13}$	$2.37^{+0.08}_{-0.06}$	$10.52^{+0.02}_{-0.02}$	$0.59^{+0.25}_{-0.20}$	$-10.76^{+0.15}_{-0.18}$	$1.92^{+0.12}_{-0.16}$	$2.09^{+0.00}_{-0.03}$
14897	$2.37^{+0.15}_{-0.14}$	$10.77^{+0.03}_{-0.03}$	$0.224^{+0.112}_{-0.071}$	$0.31^{+0.02}_{-0.01}$	$0.29^{+0.10}_{-0.12}$	$2.44^{+0.05}_{-0.07}$	$10.51^{+0.02}_{-0.03}$	$0.83^{+0.30}_{-0.24}$	$-10.60^{+0.14}_{-0.15}$	$1.75^{+0.13}_{-0.13}$	$2.33^{+0.01}_{-0.03}$
18351	$2.23^{+0.19}_{-0.20}$	$10.90^{+0.02}_{-0.03}$	$0.258^{+0.119}_{-0.067}$	$0.33^{+0.03}_{-0.02}$	$0.52^{+0.12}_{-0.13}$	$2.47^{+0.04}_{-0.04}$	$10.65^{+0.02}_{-0.02}$	$2.04^{+0.82}_{-0.66}$	$-10.33^{+0.14}_{-0.18}$	$1.59^{+0.16}_{-0.16}$	$2.08^{+0.00}_{-0.02}$
20697	$2.65^{+0.18}_{-0.29}$	$11.25^{+0.02}_{-0.03}$	$0.391^{+0.851}_{-0.181}$	$0.32^{+0.03}_{-0.02}$	$0.70^{+0.16}_{-0.45}$	$2.24^{+0.07}_{-0.04}$	$10.98^{+0.02}_{-0.02}$	$1.64^{+1.13}_{-0.89}$	$-10.77^{+0.24}_{-0.32}$	$1.98^{+0.18}_{-0.26}$	$1.63^{+0.00}_{-0.01}$
27482*	$2.39^{+0.02}_{-0.03}$	$11.09^{+0.01}_{-0.01}$	$0.194^{+0.015}_{-0.024}$	$0.30^{+0.00}_{-0.00}$	$0.78^{+0.06}_{-0.04}$	2.66	$10.83^{+0.01}_{-0.01}$	$1.23^{+0.13}_{-0.09}$	$-10.74^{+0.05}_{-0.03}$	$1.79^{+0.02}_{-0.03}$	$1.80^{+0.01}_{-0.02}$
29599	$2.30^{+0.25}_{-0.19}$	$10.34^{+0.03}_{-0.03}$	$0.242^{+0.161}_{-0.076}$	$0.32^{+0.03}_{-0.02}$	$0.45^{+0.13}_{-0.13}$	$2.33^{+0.07}_{-0.05}$	$10.08^{+0.02}_{-0.03}$	$0.43^{+0.20}_{-0.16}$	$-10.45^{+0.18}_{-0.20}$	$1.66^{+0.19}_{-0.16}$	$2.23^{+0.02}_{-0.05}$
32926	$2.34^{+0.20}_{-0.19}$	$10.23^{+0.03}_{-0.03}$	$0.191^{+0.076}_{-0.055}$	$0.33^{+0.03}_{-0.02}$	$0.10^{+0.13}_{-0.07}$	$2.47^{+0.06}_{-0.07}$	$9.97^{+0.02}_{-0.03}$	$0.30^{+0.17}_{-0.10}$	$-10.47^{+0.19}_{-0.20}$	$1.68^{+0.18}_{-0.16}$	$1.73^{+0.01}_{-0.04}$
34122*	$2.24^{+0.22}_{-0.19}$	$11.12^{+0.02}_{-0.03}$	$0.295^{+0.387}_{-0.091}$	$0.32^{+0.04}_{-0.02}$	$0.90^{+0.14}_{-0.29}$	2.50	$10.87^{+0.02}_{-0.02}$	$3.20^{+2.05}_{-1.56}$	$-10.37^{+0.23}_{-0.30}$	$1.60^{+0.21}_{-0.18}$	$1.37^{+0.00}_{-0.01}$
43489	$2.43^{+0.20}_{-0.29}$	$11.00^{+0.03}_{-0.03}$	$0.435^{+0.666}_{-0.193}$	$0.33^{+0.04}_{-0.02}$	$0.98^{+0.20}_{-0.29}$	$2.42^{+0.11}_{-0.11}$	$10.74^{+0.03}_{-0.03}$	$1.72^{+1.71}_{-0.84}$	$-10.50^{+0.29}_{-0.29}$	$1.76^{+0.20}_{-0.26}$	$1.72^{+0.03}_{-0.06}$
45378*†	$2.53^{+0.20}_{-0.26}$	$10.95^{+0.03}_{-0.03}$	$0.374^{+1.400}_{-0.184}$	$0.32^{+0.03}_{-0.01}$	$1.46^{+0.25}_{-0.59}$	2.31	$10.69^{+0.02}_{-0.02}$	$1.00^{+1.14}_{-0.53}$	$-10.70^{+0.34}_{-0.31}$	$1.88^{+0.20}_{-0.25}$	$5.50^{+0.34}_{-0.44}$
45398*	$2.54^{+0.08}_{-0.14}$	$10.37^{+0.02}_{-0.02}$	$0.242^{+0.111}_{-0.053}$	$0.31^{+0.02}_{-0.01}$	$0.81^{+0.08}_{-0.13}$	2.44	$10.10^{+0.02}_{-0.01}$	$0.21^{+0.10}_{-0.06}$	$-10.78^{+0.16}_{-0.15}$	$1.90^{+0.08}_{-0.12}$	$6.23^{+0.23}_{-0.64}$
48116*	$2.12^{+0.18}_{-0.14}$	$11.09^{+0.02}_{-0.02}$	$0.194^{+0.046}_{-0.035}$	$0.32^{+0.02}_{-0.02}$	$0.56^{+0.11}_{-0.10}$	2.59	$10.83^{+0.02}_{-0.02}$	$3.49^{+1.27}_{-0.94}$	$-10.29^{+0.13}_{-0.14}$	$1.50^{+0.14}_{-0.12}$	$2.00^{+0.07}_{-0.09}$
62921	$2.68^{+0.11}_{-0.12}$	$11.05^{+0.02}_{-0.02}$	$0.205^{+0.046}_{-0.030}$	$0.31^{+0.02}_{-0.01}$	$0.16^{+0.08}_{-0.08}$	$2.28^{+0.04}_{-0.05}$	$10.77^{+0.02}_{-0.02}$	$0.62^{+0.22}_{-0.17}$	$-10.99^{+0.15}_{-0.13}$	$2.05^{+0.10}_{-0.11}$	$1.50^{+0.00}_{-0.01}$
68318	$2.57^{+0.45}_{-0.58}$	$10.56^{+0.05}_{-0.05}$	$0.373^{+0.571}_{-0.185}$	$0.38^{+0.14}_{-0.06}$	$0.75^{+0.31}_{-0.44}$	$2.03^{+0.18}_{-0.08}$	$10.30^{+0.04}_{-0.04}$	$0.90^{+3.25}_{-0.65}$	$-10.33^{+0.67}_{-0.60}$	$1.78^{+0.47}_{-0.57}$	$1.33^{+0.00}_{-0.01}$

Note.—Values shown as median with 16th/84th percentile uncertainties: $\mathrm{value}^{+\sigma_{\rm hi}}_{-\sigma_{\rm lo}}$. All physical parameters have been derived from BAGPIPES SED fitting with delayed tau star formation history. * Indicates galaxies with confirmed spectroscopic redshifts, obtained from DJA; for these objects, the redshift error is not shown. † The BAGPIPES fit is not reliable due to bimodal posteriors; see the Appendix B for more information.

3.4 Morphological analysis using statmorph and pysersic

With our final sample defined, we turn to characterizing their structural properties to understand their physical sizes, light distributions, and overall morphologies. To achieve a comprehensive view of their structures, we employ both non-parametric measurements and parametric morphological modeling. We perform the non-parametric morphological analysis of the selected massive quiescent galaxies using the `statmorph` package [61]. `statmorph` is a Python library designed for measuring different non-parametric (CASGM) morphological statistics of galaxies in astronomical images, including concentration, asymmetry, smoothness (CAS), Gini coefficient, and the M_{20} parameter (GM). Taken together, these parameters provide insights into the structural properties of galaxies, such as their light distribution, symmetry, and clumpiness. For parametric morphological analysis, we use the `PySersic` package [62] to perform bulge-disk decomposition of the galax-

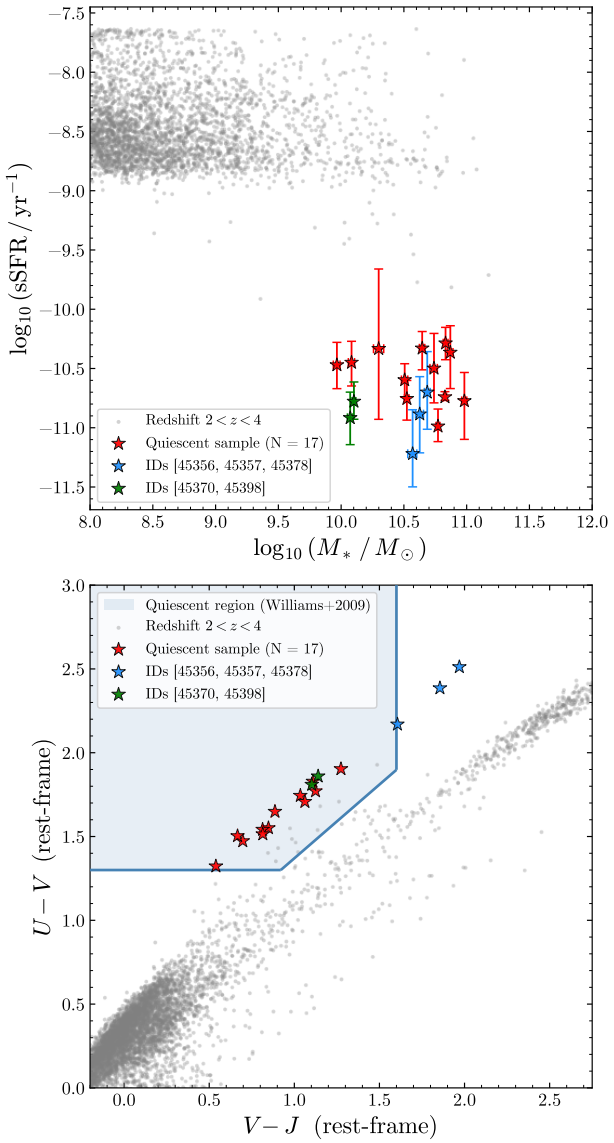

Figure 3.2: The stellar mass vs sSFR (in log scale, top panel) and UVJ diagram (bottom panel) for our sample of 17 massive quiescent galaxies out of all the galaxies in the survey with redshifts between 2 and 3. The quiescent selection boundary from Williams et al. [3] is shown in the UVJ plot, as a light-blue shaded region. The stellar mass vs sSFR plot shows that our sample galaxies lie well below the star-forming galaxies, consistent with their quiescent nature. The three multiply-lensed images of the first source (`ID_DR3` = 45356, 45357, 45378) are marked with blue stars, and the two multiply-lensed images of the second source (`ID_DR3` = 45370, 45398) are marked with green stars. The gray points represent high-redshift galaxies in the redshift range $2 < z < 4$ in the UNCOVER survey.

ies. `PySersic` is a Python library that fits Sérsic (and other) profiles to astronomical images using Bayesian inference.

Firstly, we prepare $12''$ cutouts of the broadband filter images (F070W, F090W, F115W, F150W, F200W, F277W, F356W, and F444W). We use the bCG-subtracted images (where bright cluster galaxies are subtracted from the mosaic) from the UNCOVER survey DR3 since some of the sample galaxies are near one of the bright cluster galaxies. Using the non-subtracted science image can lead to contamination and make our `statmorph` and `PySersic` fits fail due to poor sky subtraction, caused by the high flux of a nearby bright cluster galaxy. From the UNCOVER survey DR3, we also provide the PSF (Point Spread Function of the filter), inverse-variance map, and segmentation map to `statmorph` and `PySersic` in $12''$ cutouts.

Furthermore, we mask out nearby objects using the segmentation map, leading to optimal sky subtraction and better fitting of the galaxy. In our `PySersic` pipeline, we explicitly mask out pixels with invalid values in the weight maps (where weight $\leqslant 0$). These pixels are added to the mask to exclude them from the fit. As an additional safeguard, we set the RMS values for these invalid pixels to $10\times$ the median RMS of the valid pixels, ensuring they do not bias the model.

For `pysersic`, we provide all the above-mentioned inputs and fit a `sersic_exp` model to the galaxy. The `sersic_exp` model is a combination of a Sérsic [86, for the bulge] and an exponential profile (for the disk). We use the `autoprior` feature of `PySersic` to automatically set the priors for the parameters based on the input image. This feature uses `photutils` [87] to generate priors by measuring the properties of the galaxy in the image cutout. We manually give the X_c and Y_c priors, where X_c and Y_c are the x and y coordinates of the galaxy centroid respectively, in a 20×20 (for SW filters: F090W, F115W, F150W, F200W) and 10×10 (for LW filters: F277W, F356W, F444W) pixel area around the galaxy center detected by `photutils` via the `autoprior` feature, to avoid a centroiding error. For some galaxies with low SNR, we manually force the X_c and Y_c priors to be in the center of the image in case `photutils` is not able to detect the center properly. We use `sky_type` = "flat" and estimate the posterior distribution using the `svi-flow` method. `svi-flow` is a form of variational inference that uses the block neural autoregressive flow (BNAF), a normalizing flow model, to approximate the posterior distribution [88].

3.5 Spatially Resolved Analysis using piXedfit

Spatially resolved analysis is an essential part of our work because it helps us understand exactly how quenching occurs within individual galaxies. Looking at a galaxy as a single integrated object can often obscure important local details. By measuring physical properties across different regions of a galaxy, we can try to piece together its history of mass assembly and star formation. This detailed approach allows us to observationally test if mechanisms like inside-out quenching are actually responsible for shutting down star formation in these massive galaxies at cosmic noon.

We use the `piXedfit` package [63] to perform spatially resolved analysis of the selected massive quiescent galaxies. `piXedfit` is a Python package designed for pixel-by-pixel SED modeling of galaxies using multi-wavelength imaging data. It allows for the extraction of spatially resolved physical properties of galaxies, such as stellar mass, star formation rate, age, metallicity, and dust attenuation, by modeling the observed SEDs of individual pixels within a galaxy. It involves several key steps, which we describe below.

3.5.1 Creating an image datacube

Using the `piXedfit_images` module, we begin by preparing multi-wavelength imaging data of the target galaxies, ensuring that the images are aligned and have consistent pixel scales ($0.04''$). This may involve resampling and reprojecting images from different filters to a common grid. We use the F444W filter as the reference for the PSF matching. We use the PSF matching kernels from the UNCOVER DR3 [59]. We then combined the images into a datacube where each slice corresponds to a different wavelength or filter. Also, a region of interest is defined within the datacube to focus on the target galaxy using `SEP` (Source Extractor as a library) [89, 90] via `piXedfit`'s image processing module, which can add different filters' segmentation maps together to construct the segmentation map. We used the F115W, F150W, and F200W filters to construct the segmentation map. The parameters used for SEP are as follows:

- `minarea` $= 40$, minimum number of pixels above the threshold for an object to be detected.
- `thresh` $= 2.0$, detection threshold in units of the background RMS.
- `deblend_nthresh` $= 40$, number of thresholds used for deblending overlapping objects.

- `deblend_cont` $= 0.001$, minimum contrast ratio for deblending.

We use a tight deblending contrast ratio because Abell 2744 is a dense field. Additionally, two of our sample galaxies (`ID_DR3` $= 20697$ & 45378) contained foreground objects that were not deblended correctly and therefore, not included as separate objects in the UNCOVER catalog. These galaxies are distinctly visible in the shorter-wavelength filters but are faint in the longer-wavelength filters (see Figure 3.1). We assume them to be foreground galaxies and deblend them. We then run `BAGPIPES` on these foreground galaxies. They are low mass ($\log(M_*/M_\odot) \approx 8.0$ and 7.4 respectively) and at lower redshifts ($z \approx 1.4$ and 1.94 respectively). In the corner plots of the galaxy near 20697, we can see that the redshift posterior has a very small bump at $z \sim 2.1$. This is similar to the redshift of our main galaxy ($z \sim 2.24$), so there is a small probability that the foreground galaxy is actually a satellite of the main galaxy. However, the redshift posterior could also be attributed to the possibility of the main galaxy contaminating the photometry of the foreground galaxy, which could lead to a bimodal redshift posterior. We would require spectroscopic data to confirm whether it is a satellite or not. All the `piXedfit` analyses are done assuming that this object is a foreground galaxy and is therefore masked out from the main galaxy. The galaxy near 45378 has a redshift that is significantly lower than the redshift of the main galaxy ($z \sim 2.3$) with a narrow redshift posterior, so it is unlikely to be a satellite. We have also masked it out of the main galaxy in our `piXedfit` analysis.

3.5.2 Pixel Binning

For spatially resolved SED modeling, we apply pixel binning to the datacube using the `piXedfit_bin` module. This process groups neighboring pixels based on their signal-to-noise ratio (SNR), spatial proximity, and SED similarity, forming bins that preserve spatial structure while improving SNR for more robust SED modeling. The method utilizes the Voronoi binning algorithm of Cappellari and Copin [91], producing compact, non-overlapping bins with similar SNR in a chosen band. The algorithm has been modified by Abdurro'uf and Akiyama [92] to also account for SED shape similarity among pixels. The SED shape similarity helps us achieve good, consistent SED modeling for all the bins. The parameters used for pixel binning are as follows:

- `ref_band` = F200W, index of the reference band (filter) for sorting pixels based on the

brightness. The central pixel of a bin is the brightest pixel in this reference band. We use F200W as the reference band because it corresponds to the rest-frame optical wavelength for all our sample galaxies.

- `target_snr` = 5, target signal-to-noise ratio for each bin.
- `Dmin_bin` = 8 pixels, minimum size of each bin. This is high so that we get sufficient SNR in the F070W and F090W filters, even though we have not enforced a target SNR for these filters.
- `del_r` = 2 pixels, it is the increment of circular radius (in units of pixels) adopted in the pixel binning process.
- `redc_chi2_limit` = 3, reduced chi-squared threshold below which two pixels' SEDs are considered similar in shape and are added to the bin.

We set an SNR threshold for each broadband filter following Haryana et al. [8]. Here, all the filters below the rest frame wavelength of 4000 Å have the SNR threshold set to zero, with the rest of them having `target_snr` = 5. We set those filters to have a zero SNR threshold because the rest frame UV part of the SED is very faint for quiescent galaxies and thus has low SNR. On the other hand, we set the SNR threshold for all medium bands to zero, since medium bands have lower SNRs compared to the broadbands.

3.5.3 SED modeling

To fit the bins of the binned datacube, we first generate the model SEDs. This is done by using the `piXedfit_model` module. It uses the Flexible Stellar Population Synthesis (FSPS) code [93, 94] to generate the model SEDs. For interface to the Python environment, the python-fsps [95] package is used. After generating the model SEDs, we use the `piXedfit_fitting` module to fit the observed SEDs of the binned datacube with the generated model SEDs. We fix the redshifts of the bins to the redshifts of the main galaxies, derived from `BAGPIPES` or the spectroscopic redshifts, where available. The modeling is done using a Bayesian approach, which allows us to derive posterior probability distributions for the physical parameters of interest. The parameters used are mentioned

in the Table 3.2. We use the Kroupa and Boily [76] initial mass function, Padova isochrones [96, 97, 98], MILES stellar spectral library [99, 100], Calzetti et al. [101] dust law, Draine and Li [102] dust emission and nebular emission modeling [103] based on the `CLOUDY` code [104, 105]. We do not use the AGN component. Furthermore, we fix the ionization parameter to be $\log U = -3$ for the nebular emission modeling (similar to our `BAGPIPES` settings).

Using the `piXedfit` SED modeling results, we calculate the pixel-level stellar mass and SFR following Haryana et al. [8]. The pixel-level redistribution is done by weighting the flux of each pixel in a bin to the total flux of the bin in a reference band (F090W for SFR and F444W for stellar mass). We then compute the radial profiles of the stellar mass, SFR, sSFR, mass-weighted age, and dust attenuation (A_V). We extract the ellipticity and position angle of the galaxy from the `piXedfit` F200W output (PSF-matched image) using SEP, and then make the radial profiles with elliptical annuli.

Table 3.2: `piXedfit` Modeling Parameters

Parameter	Value / Range	Description
Star Formation History (Delayed Tau Model)		
log_age	[0.1, 0.6]	Log of age (Time since SF began) in Gyr
log_tau	[-1.0, 1.5]	Log of e-folding timescale of SFH decay in Gyr
logzsol	[-0.2, 0.2]	Log of stellar metallicity ($Z/Z_{\odot}$)
Dust Attenuation & Emission		
dust2	[0.0, 5.0]	ISM dust law param following Calzetti et al. [101] (Optical depth)
log_gamma	[-4.0, 0.0]	Log of dust emission parameter
log_qpah	[-3.0, 1.0]	Log of PAH abundance
log_umin	[-1.0, 1.39]	Log of minimum radiation field intensity
Nebular Emission		
gas_logu	-3.0	Log of the gas ionization parameter

Chapter 4

Results

4.1 Morphological Analysis

We utilize non-parametric statistics, specifically the Concentration (C) versus Asymmetry ($\log A$) and Gini versus M_{20} diagrams, to classify them. As defined by Conselice [4], elliptical galaxies typically have smooth, concentrated light profiles, placing them in regions of high C and low A. Disk galaxies exhibit lower concentration, while mergers are identified by very high asymmetry ($A > 0.35$). In the Gini–M_{20} plane [47, 6], early-type galaxies (E/S0/Sa) reside in regions of high Gini coefficient and low M_{20}, whereas late-type disks show lower Gini coefficients, and mergers occupy the parameter space with highly positive M_{20} values or exceptionally high Gini coefficients. Most galaxies in our sample fall into the Intermediate/S0s or Elliptical categories. On the other hand, our sample galaxies possess a significant bulge component, as evidenced by high Sérsic indices (n) and Bulge to Total luminosity ratios (B/T) derived from our `PySersic` fits (with median n ranging from $1.73^{+0.29}_{-0.39}$ in F115W to $4.25^{+1.18}_{-0.47}$ in F444W, and median B/T ranging from $0.54^{+0.07}_{-0.11}$ in F115W to $0.76^{+0.02}_{-0.06}$ in F444W). The morphological parameters for all the galaxies are presented in Appendix A, and the `statmorph` results for the F200W filter are shown in Figure 4.1. They include the disk/intermediate and the intermediate/Elliptical boundaries from Bershady et al. [5] in the $\log(A)$ vs. C diagram. The `PySersic` results for the F200W and F444W filters are shown in Figure 4.2 and Figure 4.3, respectively.

A significant subset of our sample (`ID_DR3` = 27482, 29599, 32926, 45398) represents the "standard" massive quiescent galaxy archetype. They are quite isolated, possess smooth and

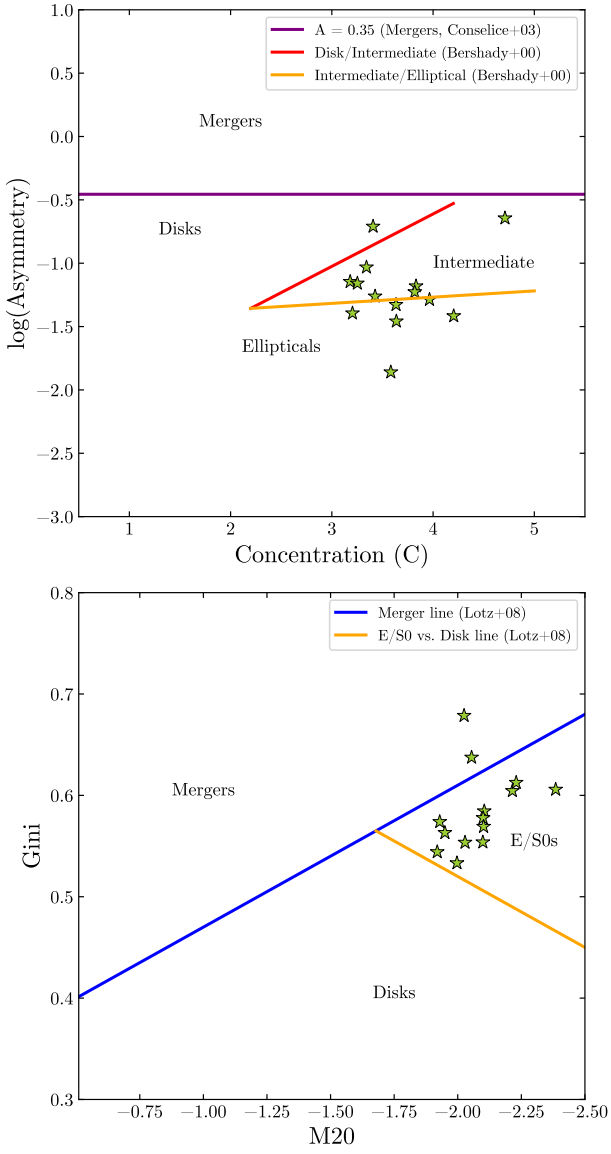

Figure 4.1: Non-parametric morphological parameters for our sample of 14 unique massive quiescent galaxies for the F200W NIRCam filter. Top: Concentration (C) vs. $\log_{10}(A)$ (asymmetry). The merger line was taken from Conselice [4], and the disk/intermediate and intermediate/elliptical boundaries were implemented following Bershady et al. [5]. Bottom: Gini coefficient vs. M_{20}. The boundary lines were implemented following Lotz et al. [6].

undisturbed morphologies, and securely reside in the Intermediate/Elliptical parameter space in almost all filters. Their PySersic fits yield very low residuals, and they are overwhelmingly bulge-dominated. ID_DR3 = 68318 (the faintest source in our sample) similarly maintains an elliptical categorization, though its lower signal-to-noise ratio introduces more scatter in its parametric (pysersic) fits.

The galaxies ID_DR3 = 14207, 14897, and 18351 demonstrate strong signs of interactions or ongoing mergers, see Figure 4.4. They often sit close to or within the merger regions of the C-log$A$ and Gini-M_{20} diagrams at shorter wavelengths. ID_DR3 = 14207 shows signs of tidal disruption with a distinct tail visible in its long-wavelength residuals (see Figure 4.3). ID_DR3 = 14897 is a compelling case of an ongoing merger, featuring two distinct cores that shift its classification toward merger and disk-dominated in short-wavelength filters (F090W and F115W) while remaining bulge-dominated at longer wavelengths. ID_DR3 = 18351 is highly disturbed with several nearby objects at similar redshifts (see Figure 4.4), resulting in predictably large Sérsic fitting residuals across all filters.

Several galaxies (ID_DR3 = 34122, 43489, 48116, 62921) exhibit complex, wavelength-dependent morphologies. They are generally classified as Intermediate/Elliptical. They are disk-dominated in the shortest wavelength filters but are bulge-dominated at longer wavelengths. ID_DR3 = 48116, in particular, displays a distinctly visible star-forming clump slightly north of its center, leading to clumpy PySersic residuals.

Inspection of the PySersic residuals occasionally reveals very faint diffraction spikes or alternating positive/negative central residuals, suggesting the presence of a point-source, in this case a very weak active galactic nucleus (AGN). These sub-structures are faintly noticeable in ID_DR3 = 14207, 14897, 27482, 43489, 48116, and 62921.

Two galaxies, ID_DR3 = 20697 and 45378, highlight edge cases caused by observational limitations. Both have nearby foreground galaxies that the UNCOVER DR3 segmentation map did not deblend. This directly affected their statmorph classifications, erroneously pushing them into the merger categories at shorter wavelengths where the foreground objects are relatively bright. Fortunately, our two-component PySersic modeling isolated the separate structures by excluding the foreground objects, resulting in clear detections in the residuals and reliable structural parameters for the target galaxies, confirming they are inherently bulge-dominated.

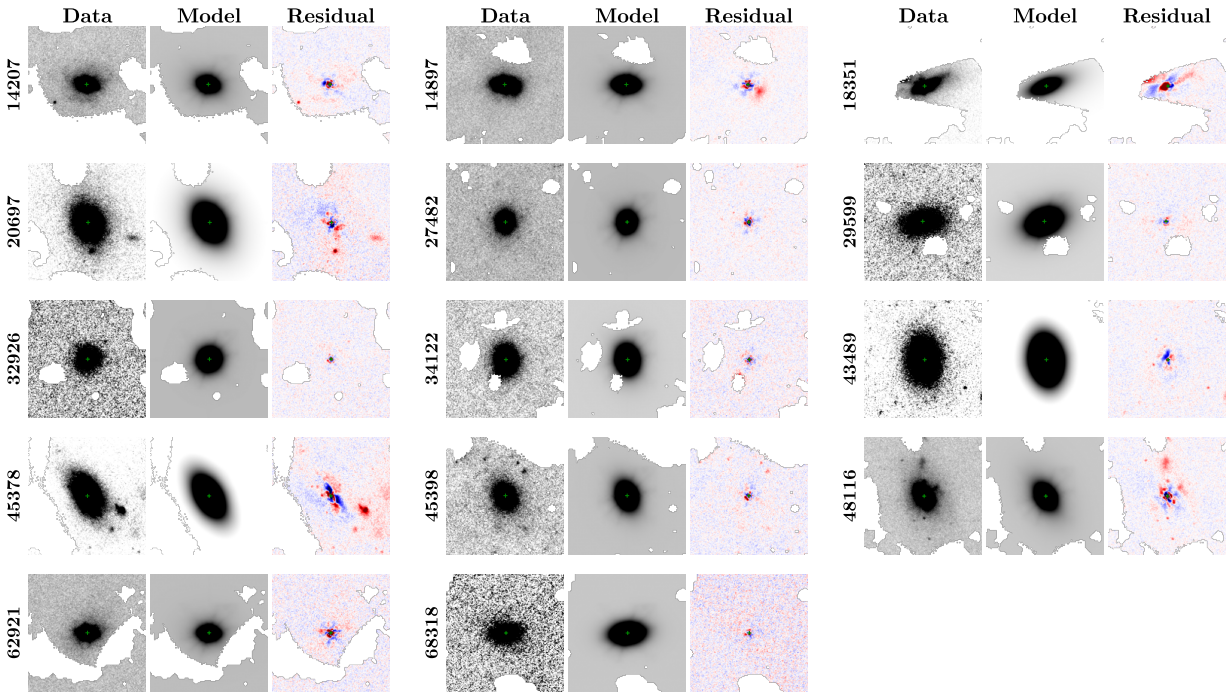

Figure 4.2: Two-component `PySersic` fits for the galaxies in our sample in the F200W filter (4″ cutouts). The panels display the original images, the median models, and the resulting residual maps. The color scale limits (vmin and vmax) for the residual plots are set to ± 0.1 (in 10 nJy), where blue regions indicate less flux than the model and red regions indicate excess flux. The average absolute residual is $4.16\% \pm 1.39\%$, with values ranging from 0.38% to 22.09%. The standard deviation of the mean is calculated via bootstrapping for 1000 iterations.

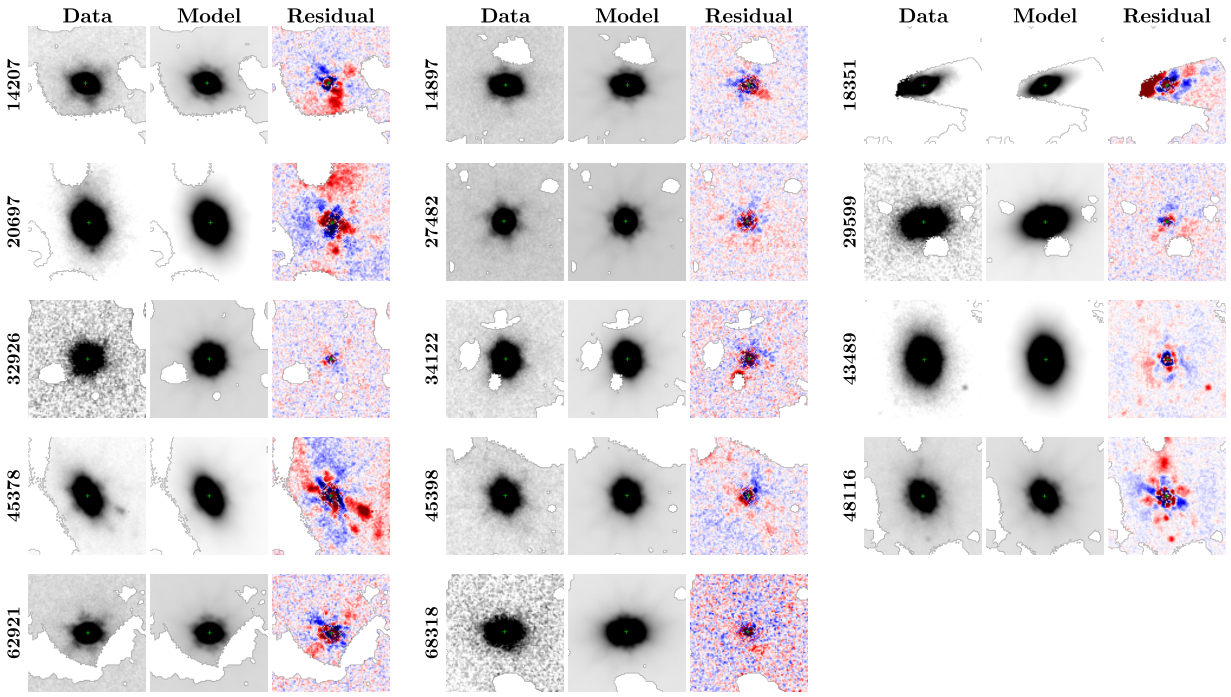

Figure 4.3: Two-component `PySersic` fits for the galaxies in our sample in the F444W filter ($4''$ cutouts). The panels display the original images, the best-fit models, and the resulting residual maps. The color scale limits (vmin and vmax) for the residual plots are set to ± 0.1 (in 10 nJy), where blue regions indicate less flux than the model and red regions indicate excess flux. The average absolute residual is $1.48\% \pm 0.67\%$, with values ranging from 0.16% to 10.25%. The standard deviation of the mean is calculated via bootstrapping for 1000 iterations.

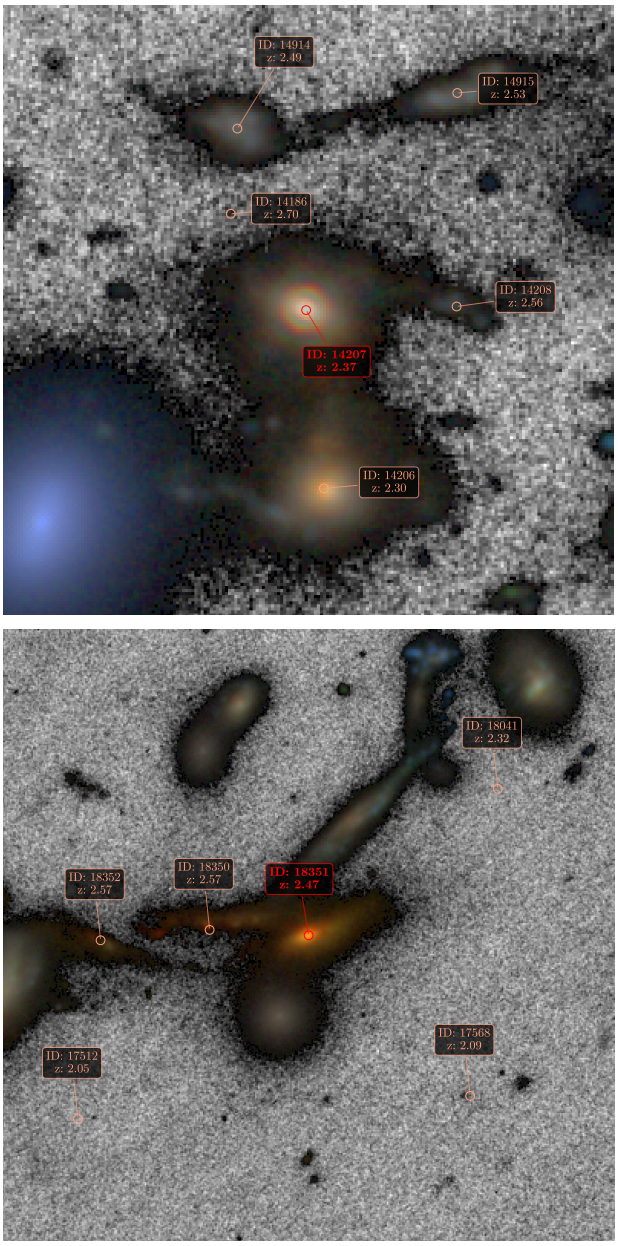

Figure 4.4: Top: This is an RGB image (using F444W, F356W, and F277W) of galaxy ID_DR3 = 14207, which is likely to have undergone tidal disruptions due to interactions with ID_DR3 = 14206, distinctly visible in the long wavelength filters. Bottom: This is an RGB image (using F200W, F150W, and F115W) of galaxy ID_DR3 = 18351, which is likely to be a merger candidate. We can see nearby objects to its left with very similar redshifts. Both the cutouts are of 8″. Surrounding galaxies with similar redshifts (obtained using BAGPIPES, within the error bars of their photometric redshifts) are marked in the cutouts.

4.2 piXedfit Analysis

Using `piXedfit`, we reconstructed spatially resolved maps of the stellar mass and SFR, and sSFR across the sample. Spatially resolved properties allow us to cleanly decouple localized structures, determine whether a galaxy is undergoing inside-out or outside-in quenching, and trace minor mergers or residual star-forming regions. Grouping our targets by their resolved spatial characteristics reveals several defining themes across the sample.

The vast majority of our sample (`ID_DR3` = 14207, 14897, 18351, 20697, 27482, 29599, 32926, 34122, 45398, 62921, 68318) exhibits a consistently positive sSFR gradient. This indicates that their inner cores are quenching faster than their outskirts, strongly supporting the inside-out quenching scenario. Within this group, smooth isolated galaxies (e.g., `ID_DR3` = 27482, 29599, 45398, and 62921) have a radial SFR profile that decreases initially but flattens or rises slightly past $\sim 2-3.5$ kpc, highlighting residual low-level star formation in their outer disks.

Three galaxies (`ID_DR3` = 43489, 45378, 48116) demonstrate ambiguous or fluctuating quenching gradients, where the sSFR visibly decreases and then increases farther out. However, their pixel-level SFR and stellar mass maps reveal a common physical driver in the form of secondary, gas-rich star-forming clumps or minor mergers. `ID_DR3` = 43489 has a secondary star-forming core towards the west of its center with ~ 2 dex lower stellar mass than the central core. Similarly, `ID_DR3` = 45378 and 48116 both feature distinctly visible off-center star-forming clumps in their SFR maps.

The spatially resolved maps also uniquely illuminate the gas and mass dynamics across our major merger candidates. For `ID_DR3` = 14207, the tidal disruption visible in the broadband images is distinctly recovered in the pixel-level stellar mass map. Interestingly, this structure is notably absent in the SFR map, suggesting the tidal interaction has primarily perturbed older stars without triggering a gas-rich starburst. On the other hand, `ID_DR3` = 14897 shows a distinctly measurable bump in its radial SFR profile at ~ 2 kpc directly corresponding to the secondary star-forming core. Finally, `ID_DR3` = 18351 shows a highly irregular SFR map and a region of high stellar mass density and dust extinction towards the left of the center, firmly establishing it as a dusty, ongoing merger with ongoing star formation.

Our `piXedfit` results for the three interacting galaxies in our sample are showcased in Fig-

ure 4.5.

4.3 Radial Profiles

We plot the mean radial profiles for the stellar mass, SFR, and sSFR for the 14 galaxies in our sample in Figure 4.6. We follow the method of Laishram et al. [7] to plot the mean radial profiles with the 68% confidence interval of the mean, derived from bootstrapping for 1000 iterations (top panel). This uses the half-mass radius (R_e) of each galaxy to normalize the radial profiles. The bins are in increments of 0.2 R/R_e. We also plot the mean radial profiles but with the R in 0.3 kpc increments instead of R/R_e (bottom panel), to enable a direct comparison with the radial profiles in Haryana et al. [8]. The overall trend matches the inside-out quenching scenario. The SFR radial profile decreases by about 1 dex near the center, then remains constant farther out. This implies that the cores of the galaxies have high star formation rates, but the decrease in stellar mass with increasing radius is faster than the decrease in SFR, leading to a positive sSFR gradient.

Additionally, we calculate the radial $U-V$ and $V-J$ radial profiles following Haryana et al. [8], shown in Figure 4.7. We define the U and V magnitudes using the filter curves computed by Maíz Apellániz [106], whereas we compute the J magnitude using the Two Micron All Sky Survey J-band transmission curve [107]. We derive the flux contribution at the pixel level by distributing the modeled U, V, and J fluxes of each bin to individual pixels. We scale them according to the observed flux in each pixel at the rest-frame wavelength of the broadband filter closest to the target band, normalized by the total observed flux within the bin.

Lastly, we compute the formation time ($t_{50,\mathrm{piX}}$) and the quenching timescale ($t_{q,\mathrm{piX}} - t_{50,\mathrm{piX}}$) radial profiles. $t_{50,\mathrm{piX}}$ is the age of the universe when the galaxy region reaches half its total mass, whereas $t_{q,\mathrm{piX}}$ is the age when its current SFR reaches 10% of its time-averaged SFR. The $t_{50,\mathrm{piX}}$ radial profiles also show a positive gradient, indicating that the inner regions (< 4 kpc) of the galaxies formed earlier than the outer regions (> 4 kpc) by ≈ 0.5 Gyr. The quenching timescale radial profiles imply that the cores of the galaxies were quenched more rapidly than the outskirts (see Figure 4.8). We also plot the Star Formation Histories (SFHs) of all the galaxies in our sample from `BAGPIPES` SED modeling in Figure 4.9. The figure also shows the quenching timescales derived from `BAGPIPES`, with the sample exhibiting a mean quenching timescale of $\Delta t_{BG} \approx 1.4$

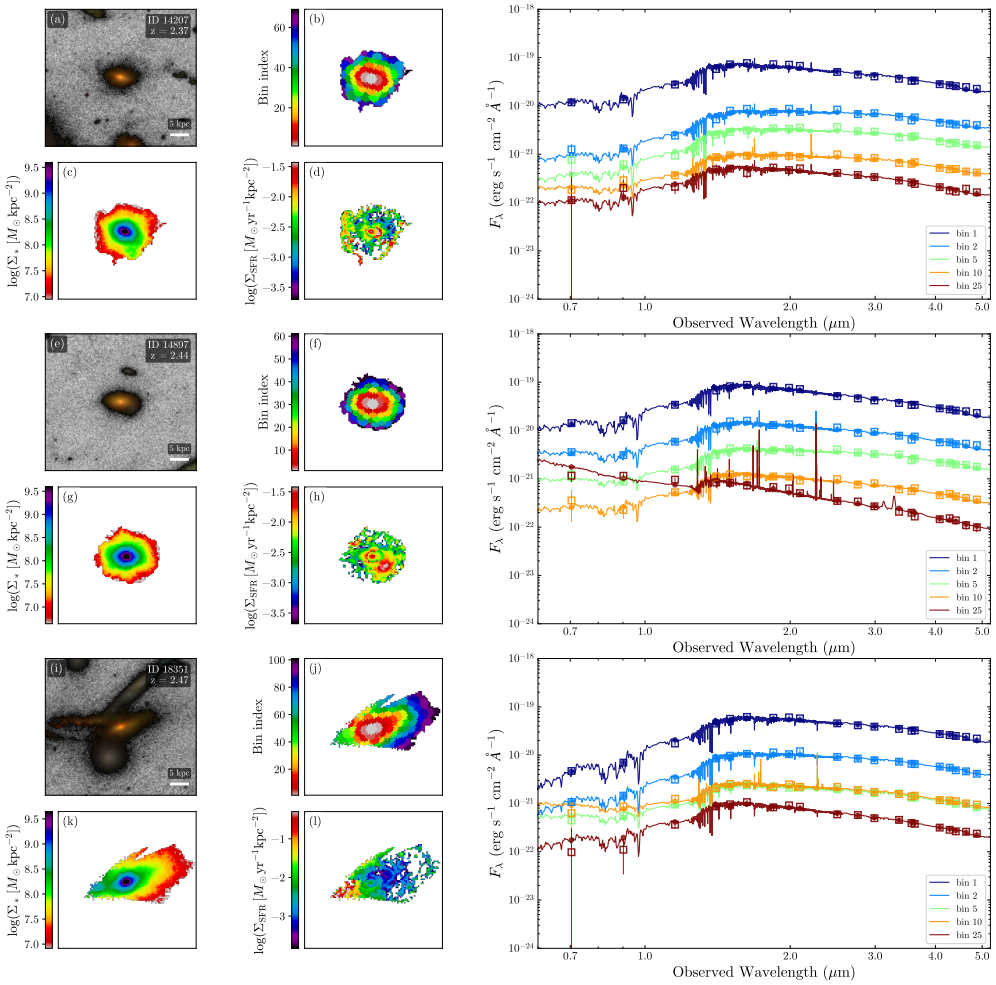

Figure 4.5: Figures (a), (e), and (i) are the RGB images (using F115W, F150W, and F200W filters), (b), (f), and (j) are the bin index maps, (c), (g), and (k) are the pixel-level stellar mass maps, and (d), (h), and (l) are the pixel-level SFR maps for the three interacting galaxies in our sample (`ID_DR3` = 14207, 14897, and 18351). The spectra of different bins for these three galaxies are shown in the figures on the right. Filled circles are the model fluxes, and the open squares are the observed fluxes, with error bars. The solid lines are the best-fit SEDs for each bin.

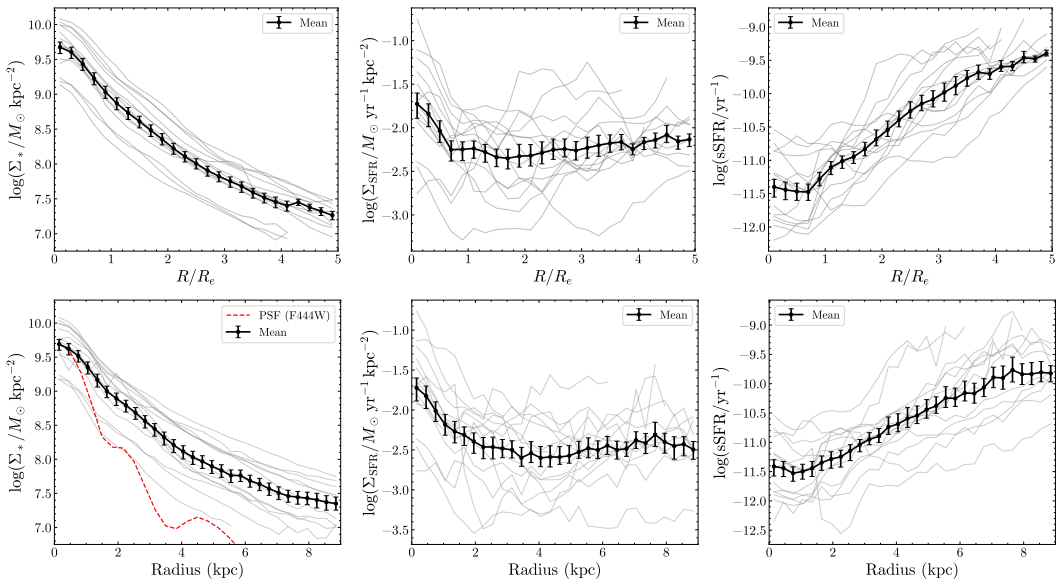

Figure 4.6: Mean radial profiles for the stellar mass, SFR, and sSFR for our sample of 14 galaxies. The top panels show the profiles normalized by the half mass radius (R_e), following Laishram et al. [7]. The bottom panels show the profiles with the radius R in increments of 0.3 kpc for direct comparison with Haryana et al. [8]. Left: Stellar mass radial profiles. Middle: SFR radial profiles. Right: sSFR radial profiles. The red dashed line in the stellar mass radial profile plot in the bottom panel is the PSF profile for the F444W filter, which is the reference filter for the PSF matching. We can observe the increasing sSFR gradient, which indicates inside-out quenching. The error bars are the 68% confidence intervals of the mean, derived from bootstrapping for 1000 iterations.

Gyr. One galaxy, `ID_DR3` = 27482, has a very short formation time ($t_{50,\mathrm{BG}} \approx 0.5$ Gyr) and very early onset of star-formation, which may be difficult to reconcile with current galaxy formation models.

All the radial profiles are similar to the trends reported in Haryana et al. [8] for their sample of 45 galaxies in redshift range $2 < z < 3$. The mean half-mass radius of our sample is $R_e = 1.95 \pm 0.13$ kpc (standard error derived via bootstrapping for 1000 iterations).

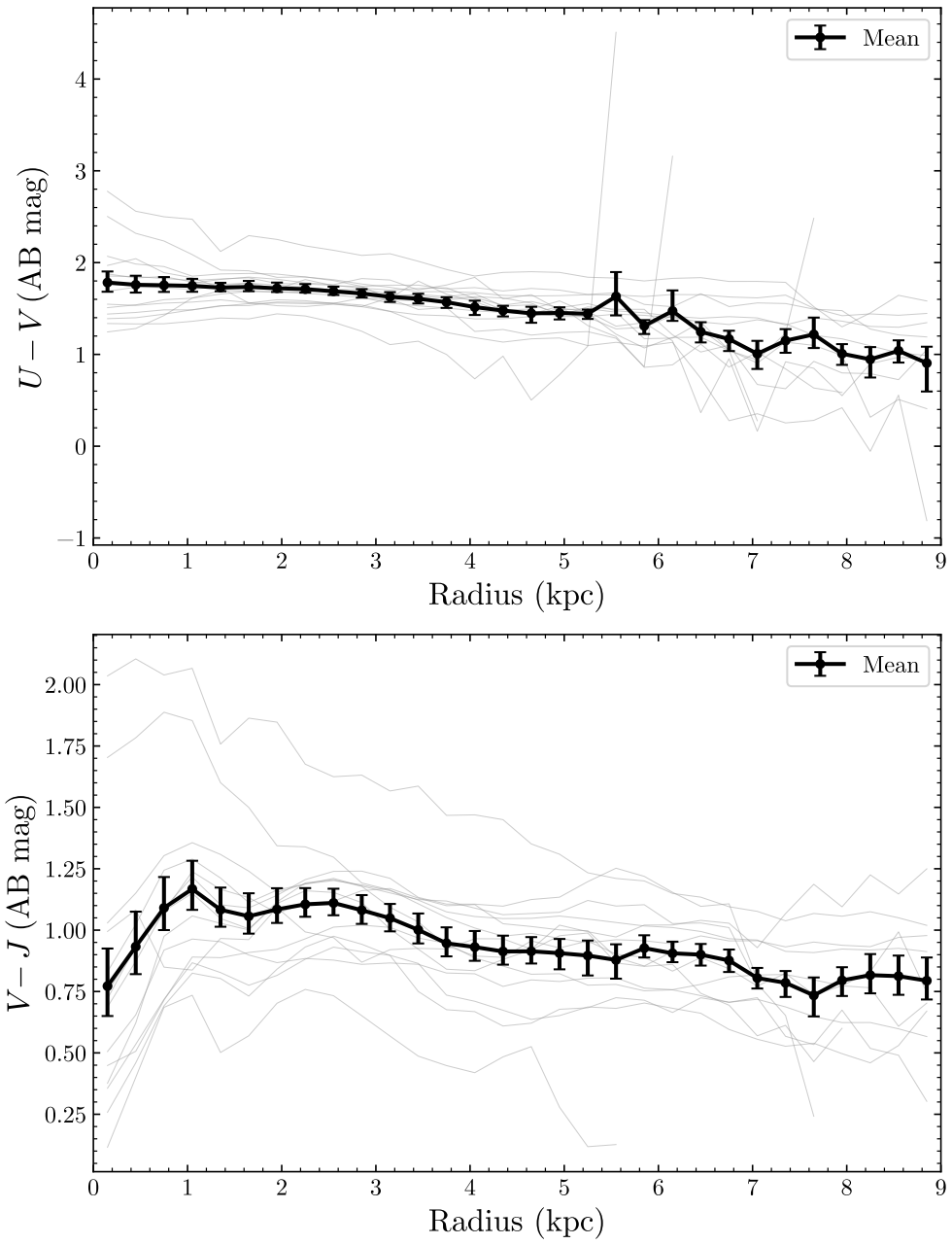

Figure 4.7: Mean radial profiles of the $U-V$ and $V-J$ colors as a function of radius in kpc for our sample of 14 galaxies. The error bars are the 68% confidence intervals of the mean, derived from bootstrapping for 1000 iterations. The profiles are derived from the `piXedfit` SED modeling.

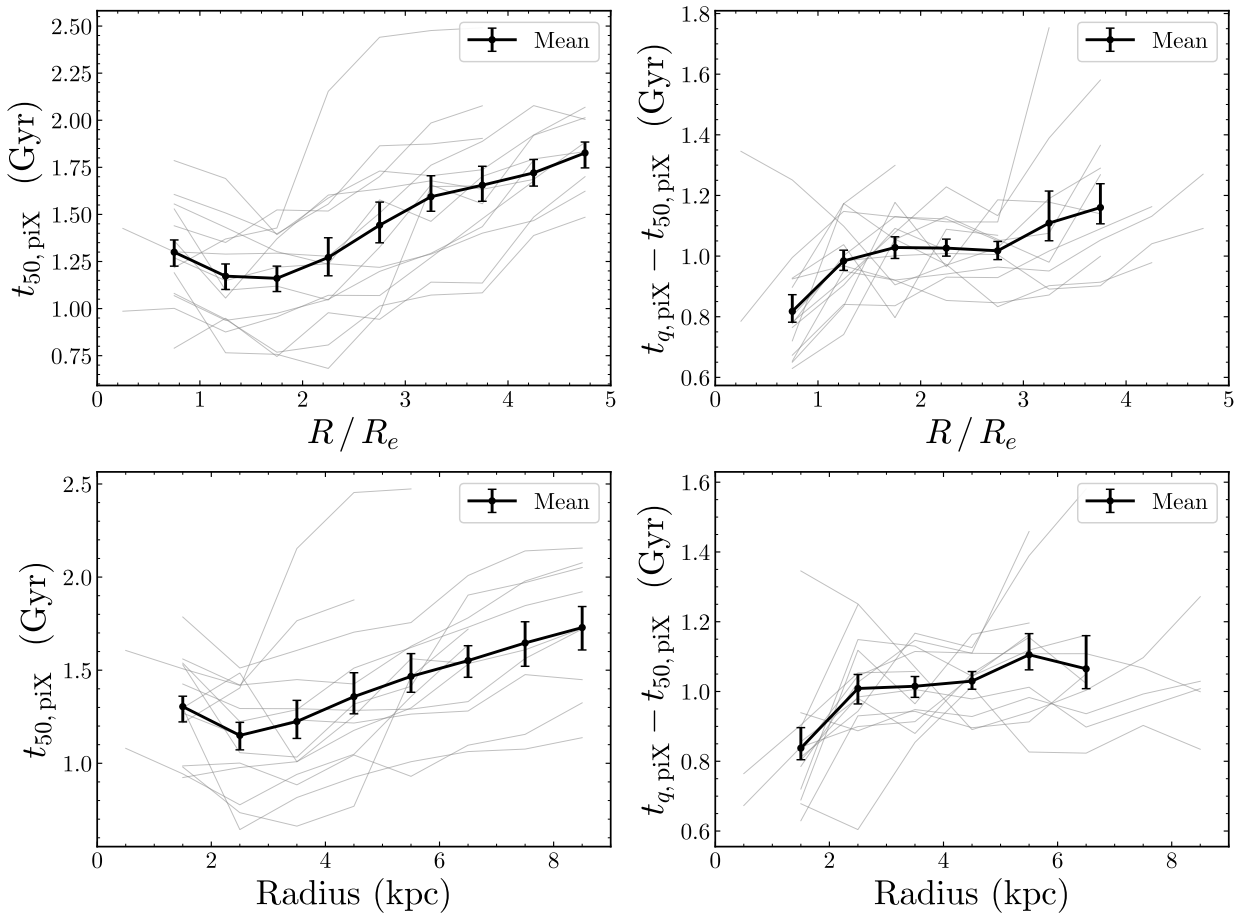

Figure 4.8: Mean radial profiles of the formation time ($t_{50,\mathrm{piX}}$, on the left) and the quenching timescale ($t_{q,\mathrm{piX}} - t_{50,\mathrm{piX}}$, on the right) for our sample of 14 galaxies. The top panels show the profile normalized by the half mass radius (R_e) in bins of 0.5 R_e, while the bottom panels show the profile with radius in kpc in bins of 1 kpc. The error bars are the 68% confidence intervals of the mean, derived from bootstrapping for 1000 iterations. The positive gradient of the formation time profile indicates that the inner regions (< 4 kpc) of the galaxies formed earlier than the outer regions (> 4 kpc) by ≈ 0.5 Gyr, whereas the quenching timescale profile implies that the cores were quenched faster than the outer regions.

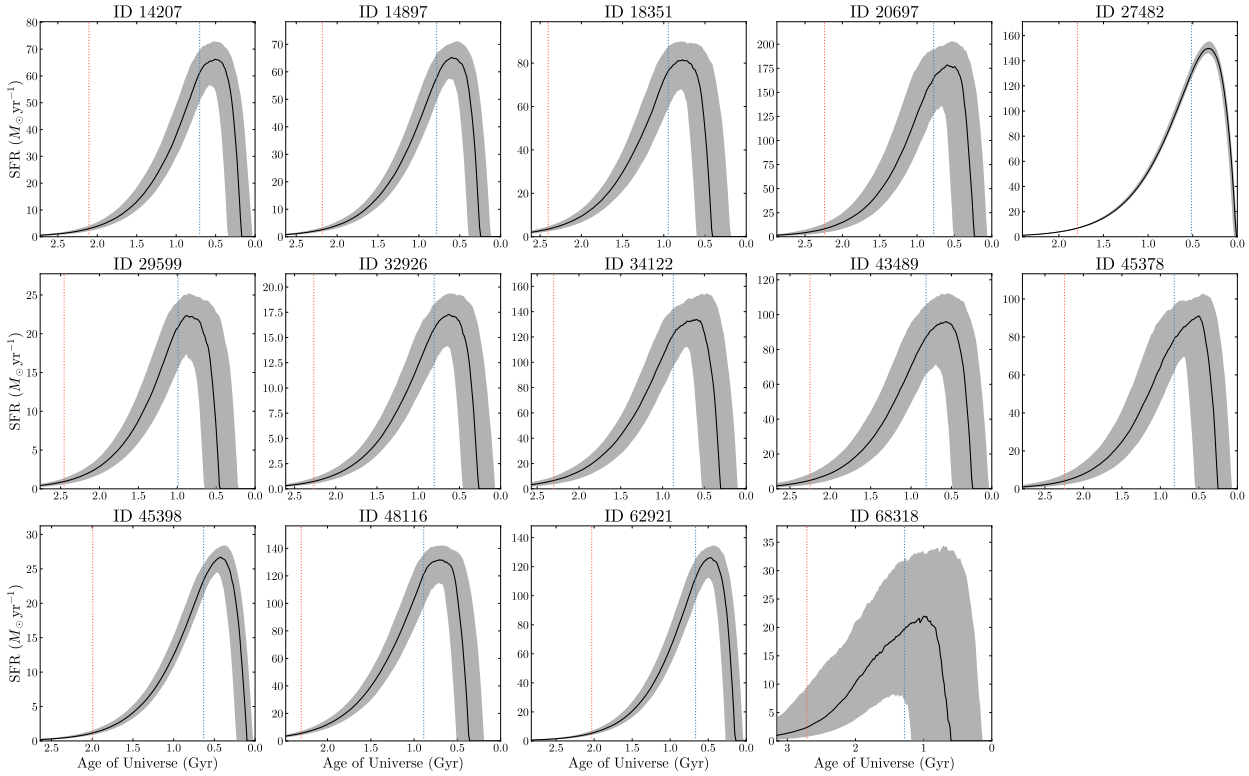

Figure 4.9: Star formation histories (SFHs) for all galaxies in our sample from BAGPIPES SED modeling. Each panel shows the posterior SFH for one galaxy, with the blue vertical line indicating the formation time ($t_{50,\mathrm{BG}}$) and the red vertical line indicating the quenching time ($t_{q,\mathrm{BG}}$). The SFHs indicate rapid early mass assembly followed by quenching in ≈ 1.4 Gyr.

Chapter 5

Discussion

In this work, we have carried out morphological analysis of our sample of massive quiescent galaxies using `statmorph` and `pysersic`. Most sample galaxies are Intermediate-type or S0s. They are also bulge-dominated in most of the filters. The Sérsic index parameterizes the galaxy's radial surface brightness profile, measuring its degree of central light concentration. While an index of $n \sim 1$ represents an exponential light profile, characteristic of a disk, higher values approaching $n \sim 4$ follow the de Vaucouleurs profile that is characteristic of classical, dispersion-dominated bulges. We plot the Sérsic indices (n) and the axis ratio (q) data from the literature in Figure 5.1, to compare with our results. We also include the F200W filter for comparison since it is closest to the rest frame optical wavelength at redshift $\sim$ 2–3. The median values of the Sérsic index and the axis ratio for our sample for various filters are given in Table 5.1. We note that 3 of our galaxies hit the upper limit of the Sérsic index in the `PySersic` fits in some filters (`ID_DR3` = 14207, 18351, and 62921, see Table A.2). Also, galaxies `ID_DR3` = 18351 and 14897 have a lower axis ratio than the rest of the sample in some filters. This could be because of the possible ongoing mergers.

To contextualize our findings, the figures also include UVJ-selected quiescent galaxies from van der Wel et al. [9], Straatman et al. [10], Ito et al. [11], photometrically selected galaxies from Marsan et al. [12], and sSFR-selected quiescent galaxies from Martorano et al. [13] for comparison across a wide redshift range. We obtained F277W n and q values from Martorano et al. [13] and cross-matched them with the COSMOS2020 catalog [14] to obtain their sSFRs. Then we applied the same sSFR selection criteria (see Equation 3.1) to the crossmatched sample. We also include the n and q (where available) of spectroscopically confirmed massive quiescent galaxies SXDS-

27434 [15, 16, 11], GS-9209 [17], RUBIES-EGS-QG-1 [18], and from Esdaile et al. [19], Lustig et al. [20], Kawinwanichakij et al. [21].

We observe that the individual points have a lot of scatter, but the median values of the Sérsic indices are around 4 for a wide range of redshift (1.5 to 4) as seen from Figure 5.1. The scatter in the n and q values could be attributed to the different selection criteria used in different works, and also to the different wavelengths at which the morphological analysis is done. Furthermore, our samples have axis ratios within error bars of the median values from other works at similar redshifts [9, 12, 20, 13]. This relatively constant $n \sim 4$ for a wide range of redshifts implies that the massive galaxies have a significant classical bulge component even at high redshifts [21].

This is an interesting result because it shows that the morphology (especially the bulge component) of a massive galaxy is linked to its quenching (and hence its sSFR) for a wide range of redshifts. Bait et al. [108] found that the morphology of a massive galaxy is strongly correlated with its sSFR, regardless of its environment, in the nearby universe. Our result supports the idea that the morphology–sSFR link is present even at high redshifts.

Transitioning to our spatially resolved analysis, from the `piXedfit` results, we find that 11 out of the 14 ($\approx 79\%$) galaxies show a positive sSFR gradient, indicating that they are quenched inside-out. The remaining 3 galaxies do not have a prominent positive or negative sSFR gradient, from which we cannot definitively say if they are quenched inside-out or outside-in. Additionally, the mean sSFR radial profiles clearly point to an inside-out quenching scenario, implying the suppression of star formation in the cores of the galaxies while the outskirts remain star-forming. The mean sSFR increases from 3.40×10^{-12} /yr at $R/R_e = 0.5$ to 3.46×10^{-10} /yr at $R/R_e = 4.5$. This is consistent with the findings of Lin et al. [54], in which they found that the fraction of massive galaxies with inside-out quenching is high irrespective of the environment in our nearby universe.

The inside-out quenching might be driven by the suppression of star formation in the cores of the galaxies due to AGN feedback [33, 32, 34] or morphological quenching [38]. Since our galaxies are massive, we believe that stellar feedback [109] does not play a major role in their quenching.

In support of morphological quenching, we also find that our sample has a high B/T ratio and Sérsic index (e.g., median n increasing from $3.49^{+0.35}_{-0.15}$ in F200W to $4.25^{+1.18}_{-0.47}$ in F444W, and

median B/T increasing from $0.66^{+0.06}_{-0.07}$ in F200W to $0.76^{+0.02}_{-0.06}$ in F444W), which has been linked to low sSFR [110, 111] and old stellar populations [112, 113, 114]. These types of galaxies tend to show inside-out quenching [54].

On the other hand, different models [115, 116, 117] and simulations [118, 119, 27] have shown that AGN feedback is necessary to quench the galaxies and to reproduce their observed properties. Inferences from simulations have also shown that AGN feedback in the form of kinetic winds is responsible for the suppression of central star formation and is required for inside-out quenching [55].

Interestingly, some galaxies in our sample have a possibility of hosting an extremely weak AGN, as indicated by the presence of faint diffraction spikes in the residuals of the `PySersic` fits. The impact of these weak AGNs on the `piXedfit` results is within 1σ uncertainties, as found by Haryana et al. [8]. For this reason, we do not use the AGN component in our `piXedfit` SED modeling. To quantify the strength of the possible AGN contribution using our imaging data, we compute the `PySersic` residuals for the central region of $0\farcs2 \times 0\farcs2$, the average absolute residual percentage is $6.73\% \pm 2.99\%$ with maximum difference of 45.74% (for `ID_DR3` = 18351; it is difficult to model it due to its disturbed morphology) with the next highest flux difference of 13.10% for the F200W filter. Similarly, the average absolute residual percentage for the F444W filter is $1.45\% \pm 0.42\%$ with a maximum difference of 6.09% with the next highest flux difference of 2.45%. So, the possible weak AGN contribution is not significant enough to affect our further analysis and conclusions. We test and find indications of the presence of a very weak AGN in some of our galaxies, which could contribute to inside-out quenching. A more detailed analysis will require follow-up observations with the NIRSpec in its MSA or IFU mode.

Our observed inside-out quenching scenario broadly aligns with recent JWST observations of rapid quenching at cosmic noon. Park et al. [35] found that massive quiescent galaxies at $z \sim 2$ show evidence of recent rapid quenching accompanied by central starbursts, where AGN activity drives multi-phase gas outflows. Similarly, Belli et al. [36] provided direct evidence for ejective AGN feedback at $z = 2.445$, detecting powerful neutral gas outflows with mass outflow rates sufficient to quench star formation. A very recent work by Scholtz et al. [37] showed that quenching is a lengthy process rather than a single mass outflow event caused by a quasar. They found that a massive quiescent galaxy at $z = 3.064$ evolved with a net-zero gas inflow, which could

have been due to a meticulous balance between inflows and outflows, with the outflows being driven by AGN feedback. A systematic future survey of the quenching mechanisms that cause a precipitous decrease in the SFR of these massive galaxies using JWST's spectroscopic capabilities will provide definitive insight into the phenomenon.

Table 5.1: Median Sérsic Index, Axis Ratio, and Bulge-to-Total Ratio Across Filters

Filter	$n_{\rm med}$	$q_{\rm med}$	$B/T_{\rm med}$
F115W	$1.73^{+0.29}_{-0.39}$	$0.71^{+0.08}_{-0.06}$	$0.54^{+0.07}_{-0.11}$
F150W	$2.35^{+0.45}_{-0.43}$	$0.74^{+0.03}_{-0.06}$	$0.63^{+0.05}_{-0.08}$
F200W	$3.49^{+0.35}_{-0.15}$	$0.75^{+0.03}_{-0.05}$	$0.66^{+0.06}_{-0.07}$
F277W	$4.20^{+0.56}_{-0.29}$	$0.62^{+0.06}_{-0.02}$	$0.67^{+0.08}_{-0.02}$
F356W	$5.43^{+0.58}_{-0.72}$	$0.65^{+0.06}_{-0.04}$	$0.75^{+0.04}_{-0.06}$
F444W	$4.25^{+1.18}_{-0.47}$	$0.64^{+0.02}_{-0.04}$	$0.76^{+0.02}_{-0.06}$

Note.—Median Sérsic index ($n_{\rm med}$), axis ratio ($q_{\rm med} = 1 - \varepsilon_{\rm bulge}$), and bulge-to-total ratio ($B/T_{\rm med}$) calculated from massive quiescent galaxies at $z \sim 2$–3 with valid pysersic fits. Sample size varies by filter: F115W (12 galaxies), F150W–F444W (14 galaxies). Uncertainties represent 68% confidence intervals ($\pm 1\sigma$) derived from bootstrap resampling with 1000 iterations. Values shown as median$^{+\Delta_{\rm hi}}_{-\Delta_{\rm lo}}$.

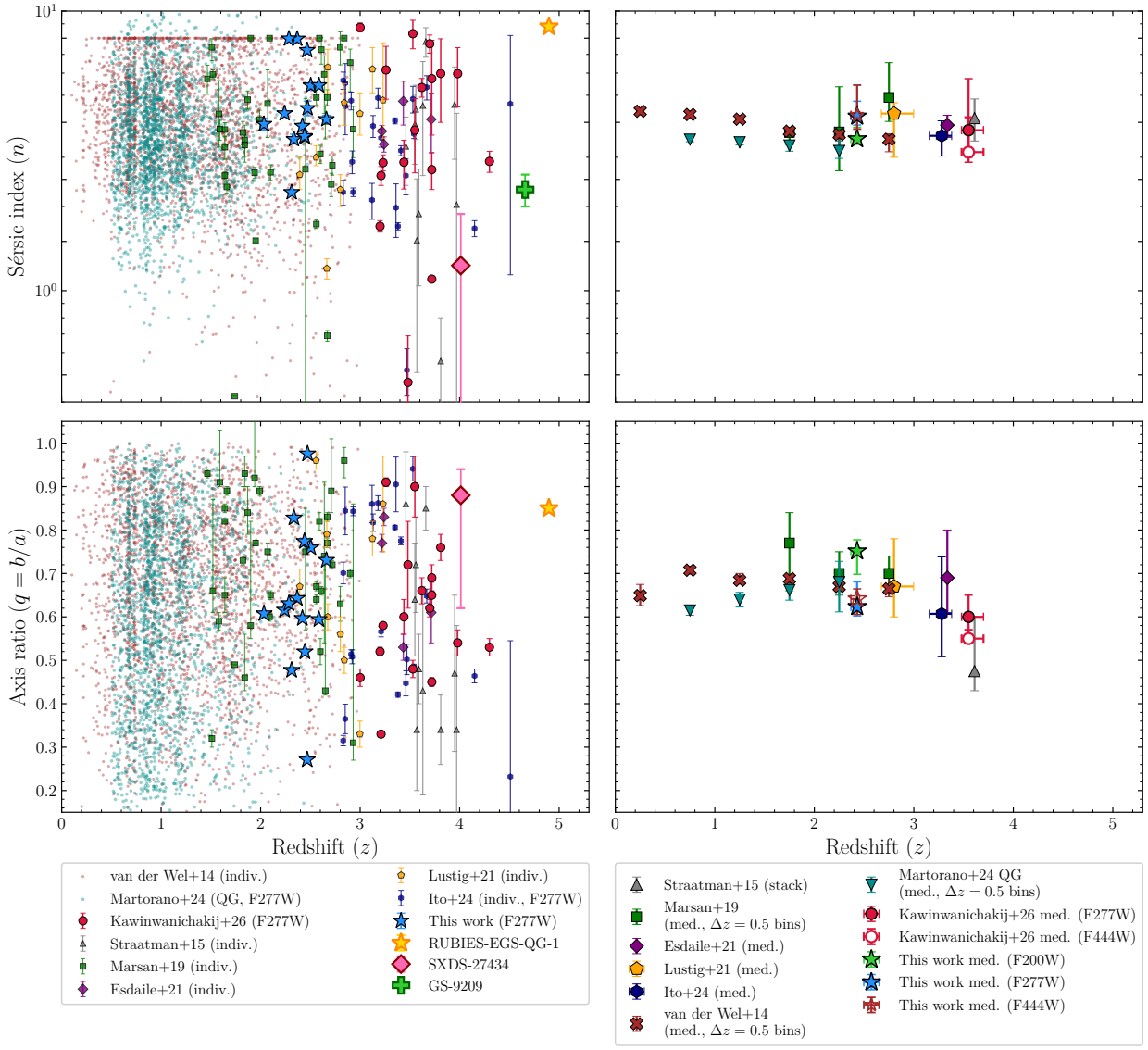

Figure 5.1: Morphological parameters as a function of redshift for our sample of massive quiescent galaxies (F277W, blue filled stars) compared with literature values. Top panels: Sérsic index (n) comparison. Bottom panels: Axis ratio (q) comparison. Comparison samples include UVJ-selected quiescent galaxies from van der Wel et al. [9, $\log(M_*/M_\odot) > 10$], Straatman et al. [10, $10.6 < \log(M_*/M_\odot) < 11.25$], and Ito et al. [11, $9.8 < \log(M_*/M_\odot) < 11.4$]; photometrically selected galaxies from Marsan et al. [12, $\log(M_*/M_\odot) > 11.25$]; and sSFR-selected quiescent galaxies from Martorano et al. [13, $\log(M_*/M_\odot) > 10$] (F277W morphology cross-matched with COSMOS2020 catalog; Weaver et al. 14). Individual spectroscopically confirmed massive quiescent galaxies are also shown: SXDS-27434 [15, 16, 11, $\log(M_*/M_\odot) = 11.06$], GS-9209 [17, $\log(M_*/M_\odot) = 10.58$], RUBIES-EGS-QG-1 [18, $\log(M_*/M_\odot) = 10.9$], and galaxies from Esdaile et al. [19, $11 < \log(M_*/M_\odot) < 11.3$], Lustig et al. [20, $10.8 < \log(M_*/M_\odot) < 11.3$] and Kawinwanichakij et al. [21, $10.2 < \log(M_*/M_\odot) < 11.2$]. On the right panels, the median Sérsic indices (top) and median axis ratios (bottom) for our sample are shown as blue-filled stars (F277W), brown-outlined stars (F444W), and green-filled stars (F200W). All the median error bars are the 68% confidence intervals derived from bootstrapping for 1000 iterations.

Chapter 6

Summary & Conclusions

We have presented a detailed analysis of the morphological and resolved star formation properties of massive quiescent galaxies at cosmic noon ($2 < z < 3$), using deep JWST NIRCam imaging from the UNCOVER Treasury program [58] and MegaScience medium-band survey [59] of the Abell 2744 lensing cluster field. Our main findings are summarized below.

1. Using `BAGPIPES` [60] SED modeling on the combined HST + JWST broadband and medium-band photometry, we select 17 massive quiescent galaxies with stellar masses $M_* \gtrsim 10^{10}\,\mathrm{M}_\odot$ and low specific star formation rates ($\mathrm{sSFR} < 0.2/t_{\mathrm{age}}$) in the redshift range $2 < z < 3$. Three of these are multiply-lensed images of the same source, and two are multiply-lensed images of another source [85, 1], giving us 14 unique galaxies for our analysis.

2. Using `statmorph` [61] and `pysersic` [62], we perform non-parametric (CAS, Gini–M_{20}) and parametric (Sérsic profile and bulge-disk decomposition) morphological analysis across all NIRCam broadband filters. Most galaxies in our sample are classified as intermediate type or S0s, with significant bulge components. The median Sérsic index is around 4, consistent with bulge-dominated systems. This value remains relatively constant across a wide redshift range ($z \sim 1.5$–4) when compared with literature values, indicating that massive quiescent galaxies had a significant bulge component already in place at high redshifts [21].

3. The persistent $n \sim 4$ across cosmic time, combined with the bulge-dominated nature of our sample, demonstrates that the morphology of massive galaxies, and in particular the bulge component, is tightly linked to their quiescence across a wide redshift range. This extends

the local-universe finding that morphology strongly correlates with sSFR regardless of environment [108] to high redshifts, suggesting that the physical processes connecting bulge growth and star formation suppression have been operating since at least $z \sim 4$.

4. From our spatially resolved SED modeling using `piXedfit` [63], 11 out of the 14 ($\sim 79\%$) galaxies show positive specific star formation rate (sSFR) gradients, with lower sSFR in the center and higher sSFR in the outskirts. This is direct evidence that these galaxies are quenching from the inside out. The mean sSFR increases by roughly two orders of magnitude from $R/R_e = 0.5$ to $R/R_e = 4.5$. The remaining 3 galaxies do not show a clearly positive or negative sSFR gradient, instead showing off-center star-forming clumps or minor mergers. Two out of the 14 galaxies have distinct secondary star-forming cores.

5. The mean radial profiles of stellar mass, SFR, and sSFR are consistent with those reported by similar studies at comparable redshifts [8, 7]. The formation time (t_{50}) radial profiles show that the inner regions (< 4 kpc) of the galaxies formed earlier than the outer regions (> 4 kpc) by approximately 0.5 Gyr, further supporting the inside-out formation and quenching scenario. The quenching timescale radial profiles indicate that the cores were quenched more rapidly than the outskirts. From `BAGPIPES` SED modeling, the mean quenching timescale ($\Delta t_{BG} = t_{q,\mathrm{BG}} - t_{50,\mathrm{BG}}$) is ≈ 1.4 Gyr, indicating rapid early mass assembly followed by efficient quenching. The mean half-mass radius of our sample is $R_e = 1.95 \pm 0.13$ kpc.

6. We find indications of the presence of a very weak AGN in some of our galaxies, identified through the presence of faint diffraction spikes in the `PySersic` residuals. The AGN contribution does not significantly affect our SED modeling results (it is within 1σ uncertainties), but the presence of possible AGN signatures is consistent with AGN-driven feedback playing a role in the quenching of these massive systems [36, 35, 37].

7. The observed inside-out quenching pattern, bulge-dominated morphologies, and the indications of very weak AGN collectively point toward AGN feedback [33, 32, 34] and morphological quenching [38] as the primary drivers of quenching in these massive systems. The high Sérsic indices and bulge-to-total ratios are linked to low sSFR and old stellar populations, consistent with the morphological quenching framework. Our findings of very weak

AGN and inside-out quenching test the results of cosmological simulations that predict AGN feedback in the form of kinetic winds as a possible mechanism for suppressing central star formation and producing inside-out quenching in massive galaxies [55].

Our results highlight the value of spatially resolved studies for understanding how quenching operates within galaxies at cosmic noon. The massive quiescent galaxies in our sample, with their established bulge components and inside-out quenching signatures, are similar to the massive elliptical galaxies we observe in the local universe. Future spectroscopic follow-up with JWST NIRSpec will be essential for confirming the role of AGN feedback through direct detection of outflows and for constraining the timescales of the quenching process in these early massive systems.

Appendix A

Statmorph and pysersic results for the 14 galaxies in our sample

This section provides the comprehensive morphological analysis results for all 14 objects in our target sample. Table A.1 summarizes the non-parametric morphological parameters, including concentration (C), asymmetry (A), smoothness (S), Gini coefficient, and M_{20}, derived using `statmorph`. Table A.2 presents the corresponding parametric Sérsic fitting results obtained with `PySersic` across multiple filters.

Table A.1: Morphological parameters from statmorph analysis across multiple filters

Filter	**ID**	C	A	S	**Gini**	M_{20}
F090W	14207	...	...	...	...	...
F115W		3.76	0.196	0.000	0.700	-2.43
F150W		3.50	0.141	0.072	0.593	-1.88
F200W		3.34	0.093	0.072	0.574	-1.93
F277W		2.99	0.058	0.000	0.537	-1.76
F356W		3.01	0.059	0.000	0.530	-1.82
F444W		3.00	0.054	0.095	0.538	-1.79
F090W	14897	4.15	0.218	0.018	0.557	-1.26
F115W		4.14	0.114	-0.026	0.617	-1.73
F150W		3.49	0.062	0.001	0.550	-2.04
F200W		3.43	0.055	0.002	0.554	-2.03
F277W		3.00	0.065	0.094	0.524	-1.88
F356W		2.90	0.054	0.090	0.513	-1.76
F444W		2.87	0.052	0.086	0.515	-1.73
F090W	18351	3.80	0.052	-2.588	0.642	-2.04
F115W		4.35	0.160	-1.085	0.691	-1.77
F150W		4.76	0.267	-0.163	0.674	-1.80
F200W		4.71	0.227	-0.023	0.679	-2.02
F277W		4.22	0.155	0.028	0.657	-2.25
F356W		4.18	0.185	0.037	0.635	-2.17
F444W		4.13	0.241	0.041	0.612	-1.80
F090W	20697	...	...	...	...	...
F115W		3.67	-0.222	-0.093	0.567	-1.29
F150W		3.97	0.069	-0.017	0.596	-2.16
F200W		3.83	0.066	-0.002	0.604	-2.21

Filter	**ID**	C	A	S	**Gini**	M_{20}
F277W		3.74	0.072	0.031	0.594	-2.19
F356W		3.55	0.051	0.038	0.572	-2.07
F444W		3.50	0.046	0.035	0.568	-2.05
F090W	27482	3.12	-0.125	-0.045	0.549	-1.91
F115W		3.40	-0.003	0.010	0.589	-2.05
F150W		3.28	0.063	-0.001	0.542	-1.94
F200W		3.20	0.040	0.001	0.544	-1.92
F277W		2.82	0.048	0.000	0.510	-1.78
F356W		2.80	0.040	0.000	0.507	-1.80
F444W		2.81	0.039	0.096	0.522	-1.74
F090W	29599	3.60	-0.074	-0.009	0.510	-2.14
F115W		3.88	-0.109	-0.041	0.582	-2.33
F150W		4.20	0.032	-0.025	0.604	-2.39
F200W		4.20	0.038	-0.006	0.606	-2.38
F277W		3.96	0.062	0.021	0.594	-2.23
F356W		3.85	0.054	0.029	0.595	-2.20
F444W		3.72	0.039	0.023	0.591	-2.11
F090W	32926	…	…	…	…	…
F115W		…	…	…	…	…
F150W		4.19	0.067	0.001	0.631	-2.24
F200W		3.82	0.059	0.025	0.584	-2.10
F277W		3.50	0.068	0.061	0.589	-1.92
F356W		3.40	0.059	0.058	0.583	-1.90
F444W		3.18	0.052	0.064	0.542	-1.84
F090W	34122	1.88	-0.286	-0.415	0.485	-0.78
F115W		3.59	-0.082	-0.052	0.596	-2.14
F150W		3.66	0.010	-0.007	0.565	-2.16
F200W		3.58	0.014	-0.004	0.554	-2.10
F277W		3.29	0.042	0.067	0.555	-1.93
F356W		3.20	0.039	0.068	0.554	-1.91
F444W		3.06	0.042	0.070	0.524	-1.86
F090W	43489	…	…	…	…	…
F115W		2.56	-0.170	-0.086	0.482	-1.30
F150W		2.94	0.038	-0.008	0.538	-1.80
F200W		3.18	0.071	0.000	0.533	-2.00
F277W		3.57	0.056	-0.001	0.568	-2.12
F356W		3.65	0.045	-0.001	0.577	-2.15
F444W		3.61	0.033	0.029	0.574	-2.10
F090W	45378	1.48	-0.110	-2.793	0.625	-0.52
F115W		1.53	0.283	0.097	0.538	-1.12
F150W		3.27	0.265	0.014	0.600	-1.90
F200W		3.41	0.195	0.012	0.637	-2.05
F277W		3.34	0.097	0.004	0.565	-1.94
F356W		3.26	0.075	0.004	0.559	-1.92
F444W		3.14	0.062	0.077	0.541	-1.92
F090W	45398	…	…	…	…	…
F115W		…	…	…	…	…
F150W		3.72	0.046	0.021	0.574	-2.15
F200W		3.64	0.035	0.027	0.578	-2.10
F277W		3.25	0.086	0.074	0.561	-1.89
F356W		3.13	0.063	0.076	0.546	-1.80
F444W		3.06	0.052	0.077	0.531	-1.81
F090W	48116	…	…	…	…	…
F115W		4.06	0.090	0.048	0.620	-2.18
F150W		3.86	0.068	0.033	0.584	-2.14
F200W		3.63	0.047	0.037	0.569	-2.10
F277W		3.22	0.037	0.091	0.550	-1.84
F356W		3.04	0.033	0.092	0.530	-1.82
F444W		2.98	0.018	0.089	0.522	-1.83
F090W	62921	…	…	…	…	…
F115W		3.36	0.075	0.061	0.555	-1.97
F150W		3.36	0.074	0.067	0.572	-1.99
F200W		3.25	0.069	0.003	0.563	-1.95
F277W		2.84	0.089	0.000	0.516	-1.74
F356W		2.85	0.086	0.000	0.520	-1.82
F444W		2.89	0.075	0.095	0.535	-1.75

Filter	ID	C	A	S	Gini	M_{20}
F090W	68318	...	...	...	...	...
F115W		3.72	0.170	0.129	0.547	-2.13
F150W		4.00	0.052	0.033	0.615	-2.23
F200W		3.96	0.052	0.015	0.613	-2.23
F277W		3.54	0.081	0.059	0.576	-2.02
F356W		3.52	0.068	0.006	0.587	-1.98
F444W		3.53	0.073	0.011	0.575	-1.93

Note.—C: concentration, *A*: asymmetry, *S*: clumpiness, M_{20}: second-order moment, *n*: Sérsic index. ... indicates measurements unavailable or flagged as unreliable.

Table A.2: Pysersic fit results across multiple filters

ID	Filter	n	θ (rad)	B/T	$r_{\rm eff,1}$ (kpc)	$r_{\rm eff,2}$ (kpc)	$q(b/a)$
14207	F090W	...	...	...	...	...	...
	F115W	$1.96^{+0.21}_{-0.20}$	$1.26^{+0.02}_{-0.02}$	$0.51^{+0.02}_{-0.02}$	$2.76^{+0.19}_{-0.19}$	$0.47^{+0.01}_{-0.01}$	$0.49^{+0.02}_{-0.02}$
	F150W	$4.85^{+0.12}_{-0.12}$	$1.29^{+0.00}_{-0.00}$	$0.68^{+0.01}_{-0.01}$	$2.75^{+0.08}_{-0.06}$	$0.79^{+0.01}_{-0.01}$	$0.62^{+0.01}_{-0.01}$
	F200W	$5.61^{+0.07}_{-0.07}$	$1.26^{+0.01}_{-0.01}$	$0.68^{+0.00}_{-0.00}$	$2.10^{+0.02}_{-0.02}$	$0.97^{+0.00}_{-0.01}$	$0.72^{+0.00}_{-0.00}$
	F277W	$7.96^{+0.02}_{-0.05}$	$1.24^{+0.00}_{-0.00}$	$0.80^{+0.00}_{-0.01}$	$1.14^{+0.02}_{-0.02}$	$1.08^{+0.01}_{-0.01}$	$0.64^{+0.01}_{-0.01}$
	F356W	$7.69^{+0.10}_{-0.16}$	$1.21^{+0.00}_{-0.00}$	$0.69^{+0.01}_{-0.01}$	$1.85^{+0.05}_{-0.05}$	$1.10^{+0.01}_{-0.01}$	$0.74^{+0.01}_{-0.01}$
	F444W	$7.95^{+0.03}_{-0.06}$	$1.20^{+0.01}_{-0.01}$	$0.77^{+0.00}_{-0.00}$	$0.99^{+0.01}_{-0.01}$	$1.08^{+0.02}_{-0.02}$	$0.66^{+0.01}_{-0.01}$
14897	F090W	$1.54^{+0.13}_{-0.10}$	$1.41^{+0.02}_{-0.02}$	$0.33^{+0.02}_{-0.02}$	$0.50^{+0.04}_{-0.03}$	$3.83^{+0.23}_{-0.21}$	$0.67^{+0.02}_{-0.02}$
	F115W	$1.50^{+0.07}_{-0.05}$	$1.48^{+0.01}_{-0.01}$	$0.43^{+0.02}_{-0.01}$	$0.50^{+0.02}_{-0.01}$	$2.52^{+0.07}_{-0.07}$	$0.68^{+0.01}_{-0.01}$
	F150W	$2.60^{+0.06}_{-0.05}$	$1.50^{+0.01}_{-0.01}$	$0.68^{+0.01}_{-0.01}$	$0.86^{+0.01}_{-0.01}$	$1.97^{+0.03}_{-0.03}$	$0.68^{+0.01}_{-0.01}$
	F200W	$3.54^{+0.05}_{-0.05}$	$1.51^{+0.00}_{-0.00}$	$0.64^{+0.01}_{-0.00}$	$1.03^{+0.01}_{-0.01}$	$1.53^{+0.01}_{-0.01}$	$0.66^{+0.00}_{-0.01}$
	F277W	$3.55^{+0.07}_{-0.07}$	$1.50^{+0.00}_{-0.00}$	$0.52^{+0.01}_{-0.01}$	$0.52^{+0.01}_{-0.01}$	$1.65^{+0.01}_{-0.01}$	$0.52^{+0.01}_{-0.01}$
	F356W	$3.62^{+0.09}_{-0.08}$	$1.49^{+0.00}_{-0.00}$	$0.51^{+0.01}_{-0.01}$	$0.49^{+0.01}_{-0.01}$	$1.61^{+0.01}_{-0.01}$	$0.55^{+0.01}_{-0.01}$
	F444W	$3.78^{+0.15}_{-0.14}$	$1.49^{+0.00}_{-0.00}$	$0.49^{+0.01}_{-0.01}$	$0.42^{+0.01}_{-0.01}$	$1.57^{+0.01}_{-0.01}$	$0.31^{+0.01}_{-0.01}$
18351	F090W	...	...	...	...	...	...
	F115W	$0.82^{+0.03}_{-0.02}$	$1.91^{+0.01}_{-0.01}$	$0.22^{+0.00}_{-0.00}$	$0.67^{+0.01}_{-0.01}$	$7.28^{+0.16}_{-0.17}$	$0.45^{+0.01}_{-0.01}$
	F150W	$3.00^{+0.10}_{-0.10}$	$1.95^{+0.01}_{-0.01}$	$0.92^{+0.01}_{-0.01}$	$7.48^{+0.15}_{-0.13}$	$4.41^{+0.27}_{-0.28}$	$0.51^{+0.01}_{-0.01}$
	F200W	$3.53^{+0.57}_{-0.18}$	$1.92^{+0.01}_{-0.01}$	$0.95^{+0.00}_{-0.00}$	$6.64^{+0.24}_{-0.25}$	$0.47^{+5.07}_{-0.13}$	$0.41^{+0.05}_{-0.01}$
	F277W	$7.25^{+0.17}_{-0.23}$	$1.91^{+0.01}_{-0.01}$	$0.65^{+0.00}_{-0.00}$	$0.87^{+0.02}_{-0.02}$	$8.19^{+0.10}_{-0.13}$	$0.27^{+0.01}_{-0.01}$
	F356W	$7.97^{+0.01}_{-0.04}$	$1.92^{+0.01}_{-0.01}$	$0.73^{+0.00}_{-0.00}$	$1.07^{+0.01}_{-0.01}$	$8.38^{+0.13}_{-0.13}$	$0.27^{+0.00}_{-0.00}$
	F444W	$7.98^{+0.01}_{-0.03}$	$1.93^{+0.00}_{-0.00}$	$0.76^{+0.00}_{-0.00}$	$0.97^{+0.01}_{-0.01}$	$8.32^{+0.09}_{-0.10}$	$0.33^{+0.01}_{-0.01}$
20697	F090W	...	...	...	...	...	...
	F115W	$4.02^{+0.24}_{-0.25}$	$0.59^{+0.04}_{-0.04}$	$0.59^{+0.04}_{-0.05}$	$2.83^{+0.29}_{-0.32}$	$5.43^{+0.28}_{-0.27}$	$0.85^{+0.03}_{-0.02}$
	F150W	$5.15^{+0.08}_{-0.08}$	$0.55^{+0.01}_{-0.01}$	$0.74^{+0.01}_{-0.01}$	$4.13^{+0.10}_{-0.09}$	$4.29^{+0.08}_{-0.08}$	$0.84^{+0.01}_{-0.01}$
	F200W	$4.62^{+0.08}_{-0.07}$	$0.51^{+0.00}_{-0.00}$	$0.82^{+0.01}_{-0.01}$	$3.49^{+0.05}_{-0.05}$	$3.95^{+0.06}_{-0.06}$	$0.78^{+0.00}_{-0.00}$
	F277W	$4.30^{+0.04}_{-0.03}$	$0.39^{+0.00}_{-0.00}$	$0.87^{+0.00}_{-0.00}$	$3.96^{+0.03}_{-0.03}$	$1.69^{+0.03}_{-0.02}$	$0.62^{+0.00}_{-0.00}$
	F356W	$5.76^{+0.04}_{-0.04}$	$0.37^{+0.00}_{-0.00}$	$0.87^{+0.00}_{-0.00}$	$3.45^{+0.02}_{-0.03}$	$2.05^{+0.02}_{-0.02}$	$0.60^{+0.00}_{-0.00}$
	F444W	$5.43^{+0.07}_{-0.07}$	$0.37^{+0.00}_{-0.00}$	$0.88^{+0.00}_{-0.00}$	$3.28^{+0.03}_{-0.03}$	$1.86^{+0.02}_{-0.02}$	$0.59^{+0.00}_{-0.00}$
27482	F090W	...	...	...	...	...	...
	F115W	$1.99^{+0.15}_{-0.15}$	$3.12^{+0.01}_{-0.02}$	$0.86^{+0.03}_{-0.03}$	$1.28^{+0.07}_{-0.07}$	$0.48^{+0.04}_{-0.04}$	$0.79^{+0.02}_{-0.02}$
	F150W	$2.80^{+0.07}_{-0.07}$	$0.02^{+0.01}_{-0.01}$	$0.66^{+0.01}_{-0.01}$	$1.20^{+0.01}_{-0.01}$	$0.83^{+0.01}_{-0.01}$	$0.82^{+0.01}_{-0.01}$
	F200W	$3.39^{+0.06}_{-0.06}$	$0.07^{+0.01}_{-0.01}$	$0.59^{+0.01}_{-0.01}$	$1.14^{+0.01}_{-0.01}$	$0.84^{+0.00}_{-0.00}$	$0.82^{+0.01}_{-0.01}$
	F277W	$4.10^{+0.13}_{-0.12}$	$0.09^{+0.01}_{-0.01}$	$0.58^{+0.01}_{-0.01}$	$0.47^{+0.01}_{-0.01}$	$0.95^{+0.01}_{-0.01}$	$0.73^{+0.01}_{-0.01}$

ID	Filter	n	θ (rad)	B/T	$r_{\rm eff,1}$ (kpc)	$r_{\rm eff,2}$ (kpc)	$q(b/a)$
	F356W	$3.83^{+0.07}_{-0.06}$	$0.17^{+0.00}_{-0.00}$	$0.64^{+0.01}_{-0.01}$	$0.52^{+0.00}_{-0.00}$	$0.85^{+0.01}_{-0.01}$	$0.67^{+0.01}_{-0.01}$
	F444W	$2.99^{+0.05}_{-0.04}$	$0.15^{+0.02}_{-0.01}$	$0.73^{+0.01}_{-0.01}$	$0.50^{+0.00}_{-0.00}$	$1.01^{+0.01}_{-0.01}$	$0.79^{+0.01}_{-0.01}$
29599	F090W	...	...	...	...	...	...
	F115W	...	...	...	...	...	...
	F150W	$1.74^{+0.06}_{-0.06}$	$1.90^{+0.01}_{-0.01}$	$0.84^{+0.00}_{-0.00}$	$3.00^{+0.05}_{-0.04}$	$0.30^{+0.01}_{-0.00}$	$0.67^{+0.01}_{-0.01}$
	F200W	$2.01^{+0.06}_{-0.06}$	$1.93^{+0.01}_{-0.01}$	$0.84^{+0.01}_{-0.01}$	$2.93^{+0.04}_{-0.04}$	$0.29^{+0.01}_{-0.01}$	$0.68^{+0.00}_{-0.00}$
	F277W	$3.48^{+0.15}_{-0.13}$	$1.81^{+0.01}_{-0.01}$	$0.49^{+0.00}_{-0.00}$	$0.50^{+0.01}_{-0.01}$	$4.51^{+0.05}_{-0.04}$	$0.83^{+0.01}_{-0.01}$
	F356W	$3.64^{+0.15}_{-0.14}$	$1.79^{+0.00}_{-0.01}$	$0.53^{+0.01}_{-0.00}$	$0.48^{+0.01}_{-0.01}$	$4.66^{+0.05}_{-0.04}$	$0.87^{+0.01}_{-0.01}$
	F444W	$3.16^{+0.21}_{-0.20}$	$1.82^{+0.01}_{-0.01}$	$0.52^{+0.01}_{-0.01}$	$0.45^{+0.01}_{-0.01}$	$4.36^{+0.05}_{-0.05}$	$0.90^{+0.01}_{-0.02}$
32926	F090W	...	...	...	...	...	...
	F115W	...	...	...	...	...	...
	F150W	$2.00^{+0.11}_{-0.09}$	$2.58^{+0.06}_{-0.06}$	$0.51^{+0.01}_{-0.01}$	$0.43^{+0.02}_{-0.01}$	$2.24^{+0.08}_{-0.07}$	$0.88^{+0.01}_{-0.01}$
	F200W	$2.13^{+0.12}_{-0.09}$	$2.76^{+0.07}_{-0.08}$	$0.55^{+0.01}_{-0.01}$	$0.49^{+0.01}_{-0.01}$	$2.22^{+0.04}_{-0.04}$	$0.94^{+0.01}_{-0.01}$
	F277W	$4.49^{+0.28}_{-0.27}$	$2.34^{+0.38}_{-1.05}$	$0.65^{+0.00}_{-0.00}$	$0.38^{+0.00}_{-0.01}$	$2.22^{+0.06}_{-0.07}$	$0.98^{+0.01}_{-0.01}$
	F356W	$6.40^{+0.26}_{-0.26}$	$2.07^{+0.49}_{-0.97}$	$0.78^{+0.00}_{-0.00}$	$0.54^{+0.01}_{-0.01}$	$2.21^{+0.08}_{-0.09}$	$0.99^{+0.00}_{-0.01}$
	F444W	$3.96^{+0.53}_{-0.53}$	$0.37^{+2.58}_{-0.25}$	$0.64^{+0.02}_{-0.02}$	$0.32^{+0.02}_{-0.02}$	$2.11^{+0.06}_{-0.06}$	$0.95^{+0.01}_{-0.02}$
34122	F090W	...	...	...	...	...	...
	F115W	$0.97^{+0.10}_{-0.09}$	$0.19^{+0.03}_{-0.03}$	$0.21^{+0.02}_{-0.02}$	$0.42^{+0.03}_{-0.03}$	$2.35^{+0.08}_{-0.09}$	$0.73^{+0.03}_{-0.03}$
	F150W	$1.20^{+0.04}_{-0.04}$	$0.22^{+0.01}_{-0.01}$	$0.26^{+0.01}_{-0.01}$	$0.45^{+0.01}_{-0.01}$	$2.23^{+0.02}_{-0.02}$	$0.77^{+0.01}_{-0.01}$
	F200W	$3.44^{+0.05}_{-0.05}$	$0.19^{+0.01}_{-0.01}$	$0.69^{+0.01}_{-0.01}$	$1.16^{+0.02}_{-0.01}$	$2.26^{+0.02}_{-0.03}$	$0.78^{+0.01}_{-0.01}$
	F277W	$5.42^{+0.20}_{-0.20}$	$0.21^{+0.00}_{-0.01}$	$0.62^{+0.00}_{-0.00}$	$0.73^{+0.01}_{-0.01}$	$2.00^{+0.02}_{-0.02}$	$0.76^{+0.01}_{-0.01}$
	F356W	$5.27^{+0.14}_{-0.14}$	$0.21^{+0.00}_{-0.00}$	$0.66^{+0.00}_{-0.00}$	$0.72^{+0.01}_{-0.01}$	$2.07^{+0.02}_{-0.02}$	$0.87^{+0.01}_{-0.01}$
	F444W	$4.55^{+0.18}_{-0.19}$	$0.21^{+0.00}_{-0.01}$	$0.65^{+0.01}_{-0.01}$	$0.66^{+0.02}_{-0.02}$	$2.05^{+0.02}_{-0.02}$	$0.84^{+0.01}_{-0.02}$
43489	F090W	...	...	...	...	...	...
	F115W	$4.45^{+0.88}_{-0.83}$	$0.19^{+0.04}_{-0.03}$	$0.06^{+0.03}_{-0.02}$	$8.35^{+1.24}_{-1.04}$	$4.10^{+0.11}_{-0.12}$	$0.80^{+0.14}_{-0.19}$
	F150W	$1.74^{+0.11}_{-0.10}$	$0.22^{+0.01}_{-0.01}$	$0.23^{+0.02}_{-0.02}$	$2.45^{+0.16}_{-0.16}$	$4.93^{+0.07}_{-0.07}$	$0.99^{+0.01}_{-0.01}$
	F200W	$4.14^{+0.14}_{-0.13}$	$0.17^{+0.00}_{-0.00}$	$0.35^{+0.01}_{-0.01}$	$3.54^{+0.12}_{-0.12}$	$4.09^{+0.03}_{-0.03}$	$0.92^{+0.02}_{-0.02}$
	F277W	$3.88^{+0.10}_{-0.10}$	$0.16^{+0.00}_{-0.00}$	$0.76^{+0.00}_{-0.00}$	$5.60^{+0.10}_{-0.13}$	$2.64^{+0.07}_{-0.06}$	$0.60^{+0.00}_{-0.00}$
	F356W	$4.61^{+0.10}_{-0.10}$	$0.15^{+0.00}_{-0.00}$	$0.82^{+0.00}_{-0.00}$	$4.55^{+0.06}_{-0.07}$	$2.61^{+0.05}_{-0.05}$	$0.62^{+0.00}_{-0.00}$
	F444W	$6.95^{+0.11}_{-0.13}$	$0.15^{+0.00}_{-0.00}$	$0.83^{+0.00}_{-0.00}$	$4.55^{+0.06}_{-0.05}$	$2.71^{+0.03}_{-0.03}$	$0.62^{+0.00}_{-0.00}$
45378	F090W	...	...	...	...	...	...
	F115W	$1.06^{+0.10}_{-0.10}$	$0.60^{+0.01}_{-0.01}$	$0.63^{+0.02}_{-0.03}$	$5.54^{+0.35}_{-0.28}$	$2.69^{+0.08}_{-0.08}$	$0.61^{+0.03}_{-0.03}$
	F150W	$0.65^{+0.00}_{-0.00}$	$0.57^{+0.00}_{-0.00}$	$0.28^{+0.00}_{-0.00}$	$1.90^{+0.02}_{-0.02}$	$5.30^{+0.05}_{-0.06}$	$0.31^{+0.00}_{-0.00}$
	F200W	$0.70^{+0.01}_{-0.01}$	$0.53^{+0.00}_{-0.00}$	$0.36^{+0.00}_{-0.00}$	$1.64^{+0.02}_{-0.02}$	$5.31^{+0.06}_{-0.08}$	$0.41^{+0.00}_{-0.00}$
	F277W	$2.25^{+0.02}_{-0.02}$	$0.53^{+0.00}_{-0.00}$	$0.80^{+0.00}_{-0.00}$	$2.97^{+0.01}_{-0.01}$	$1.28^{+0.01}_{-0.01}$	$0.48^{+0.00}_{-0.00}$
	F356W	$2.69^{+0.03}_{-0.02}$	$0.51^{+0.00}_{-0.00}$	$0.93^{+0.00}_{-0.00}$	$1.80^{+0.00}_{-0.00}$	$4.42^{+0.12}_{-0.13}$	$0.43^{+0.00}_{-0.00}$
	F444W	$3.24^{+0.02}_{-0.02}$	$0.49^{+0.00}_{-0.00}$	$0.87^{+0.00}_{-0.00}$	$1.82^{+0.00}_{-0.00}$	$1.83^{+0.02}_{-0.02}$	$0.47^{+0.00}_{-0.00}$
45398	F090W	...	...	...	...	...	...
	F115W	$1.35^{+0.18}_{-0.14}$	$0.39^{+0.05}_{-0.05}$	$0.71^{+0.02}_{-0.03}$	$2.06^{+0.15}_{-0.12}$	$0.33^{+0.01}_{-0.01}$	$0.68^{+0.03}_{-0.03}$
	F150W	$2.10^{+0.09}_{-0.09}$	$0.36^{+0.01}_{-0.01}$	$0.60^{+0.02}_{-0.02}$	$0.62^{+0.03}_{-0.02}$	$3.07^{+0.10}_{-0.10}$	$0.85^{+0.01}_{-0.01}$
	F200W	$2.83^{+0.04}_{-0.04}$	$0.36^{+0.01}_{-0.01}$	$0.77^{+0.01}_{-0.01}$	$0.89^{+0.01}_{-0.01}$	$3.20^{+0.08}_{-0.08}$	$0.82^{+0.00}_{-0.00}$
	F277W	$3.57^{+0.13}_{-0.14}$	$0.39^{+0.01}_{-0.01}$	$0.64^{+0.00}_{-0.00}$	$0.49^{+0.01}_{-0.01}$	$2.26^{+0.03}_{-0.03}$	$0.77^{+0.01}_{-0.01}$
	F356W	$4.71^{+0.08}_{-0.09}$	$0.38^{+0.00}_{-0.00}$	$0.80^{+0.00}_{-0.00}$	$0.77^{+0.01}_{-0.01}$	$2.12^{+0.03}_{-0.03}$	$0.73^{+0.01}_{-0.01}$
	F444W	$3.79^{+0.06}_{-0.06}$	$0.37^{+0.01}_{-0.01}$	$0.79^{+0.00}_{-0.00}$	$0.73^{+0.01}_{-0.01}$	$2.27^{+0.04}_{-0.04}$	$0.66^{+0.00}_{-0.00}$

ID	Filter	n	θ (rad)	B/T	$r_{\rm eff,1}$ (kpc)	$r_{\rm eff,2}$ (kpc)	$q(b/a)$
48116	F090W	$3.44^{+0.18}_{-0.17}$	$0.17^{+0.02}_{-0.02}$	$0.57^{+0.01}_{-0.01}$	$0.35^{+0.01}_{-0.01}$	$7.61^{+0.53}_{-0.53}$	$0.96^{+0.01}_{-0.02}$
	F115W	$2.50^{+0.06}_{-0.06}$	$0.44^{+0.02}_{-0.02}$	$0.63^{+0.00}_{-0.01}$	$0.47^{+0.01}_{-0.01}$	$5.08^{+0.22}_{-0.22}$	$0.86^{+0.01}_{-0.01}$
	F150W	$3.56^{+0.06}_{-0.06}$	$0.58^{+0.00}_{-0.01}$	$0.84^{+0.00}_{-0.00}$	$2.01^{+0.02}_{-0.02}$	$0.47^{+0.01}_{-0.01}$	$0.65^{+0.00}_{-0.00}$
	F200W	$4.15^{+0.04}_{-0.04}$	$0.56^{+0.00}_{-0.00}$	$0.81^{+0.00}_{-0.00}$	$1.93^{+0.02}_{-0.01}$	$0.80^{+0.01}_{-0.01}$	$0.62^{+0.00}_{-0.00}$
	F277W	$5.42^{+0.07}_{-0.07}$	$0.56^{+0.00}_{-0.00}$	$0.87^{+0.00}_{-0.00}$	$1.12^{+0.00}_{-0.00}$	$1.43^{+0.02}_{-0.02}$	$0.59^{+0.00}_{-0.00}$
	F356W	$6.27^{+0.08}_{-0.08}$	$0.55^{+0.00}_{-0.00}$	$0.82^{+0.00}_{-0.00}$	$1.05^{+0.01}_{-0.01}$	$1.39^{+0.02}_{-0.02}$	$0.62^{+0.00}_{-0.00}$
	F444W	$7.34^{+0.07}_{-0.07}$	$0.57^{+0.00}_{-0.00}$	$0.76^{+0.00}_{-0.00}$	$0.95^{+0.00}_{-0.00}$	$1.42^{+0.01}_{-0.01}$	$0.62^{+0.00}_{-0.00}$
62921	F090W	$2.35^{+0.11}_{-0.11}$	$1.42^{+0.01}_{-0.02}$	$0.49^{+0.05}_{-0.06}$	$0.95^{+0.03}_{-0.03}$	$68.90^{+3.38}_{-3.13}$	$0.56^{+0.01}_{-0.01}$
	F115W	$2.05^{+0.04}_{-0.04}$	$1.44^{+0.01}_{-0.01}$	$0.58^{+0.04}_{-0.06}$	$0.88^{+0.01}_{-0.01}$	$68.75^{+3.02}_{-2.89}$	$0.54^{+0.00}_{-0.00}$
	F150W	$5.80^{+0.23}_{-0.20}$	$1.44^{+0.00}_{-0.01}$	$0.59^{+0.00}_{-0.00}$	$1.61^{+0.09}_{-0.07}$	$1.01^{+0.01}_{-0.01}$	$0.72^{+0.01}_{-0.01}$
	F200W	$6.00^{+0.17}_{-0.15}$	$1.45^{+0.00}_{-0.00}$	$0.58^{+0.00}_{-0.00}$	$1.54^{+0.04}_{-0.03}$	$1.04^{+0.01}_{-0.01}$	$0.76^{+0.01}_{-0.01}$
	F277W	$7.97^{+0.02}_{-0.04}$	$1.48^{+0.00}_{-0.00}$	$0.68^{+0.00}_{-0.00}$	$0.71^{+0.01}_{-0.01}$	$1.13^{+0.01}_{-0.01}$	$0.63^{+0.01}_{-0.01}$
	F356W	$7.97^{+0.02}_{-0.04}$	$1.46^{+0.00}_{-0.00}$	$0.63^{+0.00}_{-0.01}$	$0.76^{+0.02}_{-0.01}$	$1.07^{+0.01}_{-0.01}$	$0.67^{+0.01}_{-0.01}$
	F444W	$7.89^{+0.05}_{-0.10}$	$1.48^{+0.00}_{-0.00}$	$0.59^{+0.01}_{-0.01}$	$0.77^{+0.02}_{-0.02}$	$1.01^{+0.01}_{-0.01}$	$0.71^{+0.01}_{-0.01}$
68318	F090W	...	...	...	...	...	...
	F115W	$0.81^{+0.11}_{-0.07}$	$1.64^{+0.05}_{-0.05}$	$0.25^{+0.03}_{-0.03}$	$0.44^{+0.04}_{-0.04}$	$2.86^{+0.21}_{-0.21}$	$0.82^{+0.04}_{-0.05}$
	F150W	$1.42^{+0.07}_{-0.06}$	$1.62^{+0.02}_{-0.02}$	$0.40^{+0.01}_{-0.01}$	$0.58^{+0.02}_{-0.02}$	$3.48^{+0.10}_{-0.10}$	$0.76^{+0.02}_{-0.01}$
	F200W	$1.15^{+0.04}_{-0.04}$	$1.65^{+0.01}_{-0.01}$	$0.38^{+0.01}_{-0.01}$	$0.50^{+0.01}_{-0.01}$	$2.88^{+0.06}_{-0.06}$	$0.75^{+0.01}_{-0.01}$
	F277W	$3.94^{+0.19}_{-0.19}$	$1.60^{+0.01}_{-0.01}$	$0.74^{+0.01}_{-0.01}$	$1.15^{+0.03}_{-0.03}$	$3.35^{+0.18}_{-0.14}$	$0.61^{+0.01}_{-0.01}$
	F356W	$5.59^{+0.18}_{-0.20}$	$1.58^{+0.01}_{-0.01}$	$0.77^{+0.01}_{-0.01}$	$0.85^{+0.02}_{-0.02}$	$3.47^{+0.14}_{-0.11}$	$0.60^{+0.01}_{-0.01}$
	F444W	$2.83^{+0.16}_{-0.17}$	$1.59^{+0.01}_{-0.01}$	$0.79^{+0.01}_{-0.01}$	$2.16^{+0.05}_{-0.06}$	$0.19^{+0.02}_{-0.01}$	$0.58^{+0.01}_{-0.01}$

Note.—Values shown as median with 16th/84th percentile uncertainties: value$^{+\sigma_{\rm hi}}_{-\sigma_{\rm lo}}$. n: Sérsic index, θ: position angle (rad), B/T: bulge to total luminosity ratio, $r_{\rm eff,1/2}$: effective radii (kpc), $q(b/a)$: axis ratio.

Appendix B

The three lensed galaxies (Source 67)

The three lensed galaxies, ID_DR3 = 45356, 45357, and 45378, do not have reliable SED modeling results due to bimodal BAGPIPES posteriors in some parameters. We include the analysis of ID_DR3 = 45378 since it has been confirmed to be a massive quiescent galaxy by Siegel et al. [85].

Figure B.1 shows the BAGPIPES posterior corner plots for each of the three lensed images, illustrating the bimodal posteriors leading to unreliable parameter estimates.

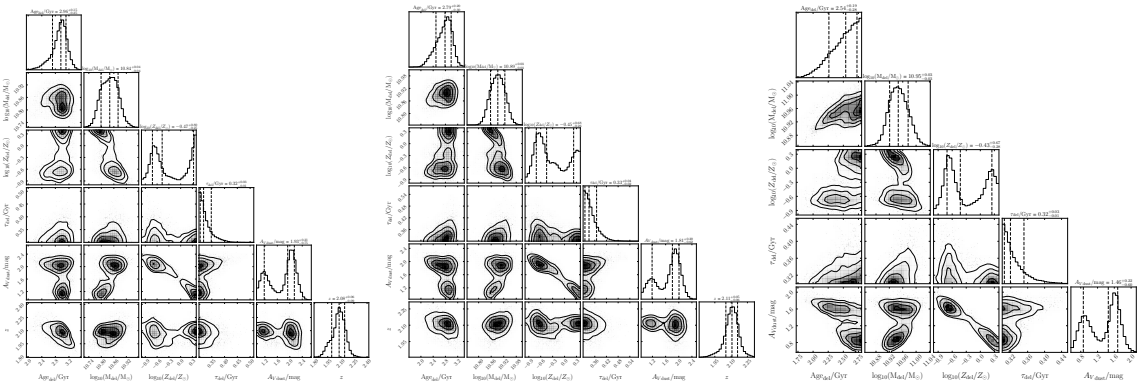

Figure B.1: BAGPIPES posterior corner plots for the three lensed images of the same galaxy: ID_DR3 = 45356 (left), 45357 (center), and 45378 (right). The bimodal posteriors in metallicity and dust (A_V) are clearly visible.

Bibliography

[1] Lukas J. Furtak, Adi Zitrin, John R. Weaver, Hakim Atek, Rachel Bezanson, et al. UNCOVERing the extended strong lensing structures of Abell 2744 with the deepest JWST imaging. *MNRAS*, 523(3):4568–4582, August 2023. doi:10.1093/mnras/stad1627.

[2] JWST User Documentation (JDox), January 2016.

[3] Rik J. Williams, Ryan F. Quadri, Marijn Franx, Pieter van Dokkum, and Ivo Labbé. Detection of Quiescent Galaxies in a Bicolor Sequence from Z = 0-2. *ApJ*, 691(2):1879–1895, February 2009. doi:10.1088/0004-637X/691/2/1879.

[4] Christopher J. Conselice. The Relationship between Stellar Light Distributions of Galaxies and Their Formation Histories. *ApJS*, 147(1):1–28, July 2003. doi:10.1086/375001.

[5] Matthew A. Bershady, Anna Jangren, and Christopher J. Conselice. Structural and photometric classification of galaxies. i. calibration based on a nearby galaxy sample. *The Astronomical Journal*, 119(6):2645, 06 2000. doi:10.1086/301386.

[6] Jennifer M. Lotz, M. Davis, S. M. Faber, P. Guhathakurta, S. Gwyn, et al. The Evolution of Galaxy Mergers and Morphology at $z < 1.2$ in the Extended Groth Strip. *ApJ*, 672(1): 177–197, January 2008. doi:10.1086/523659.

[7] Ronaldo Laishram, Yusei Koyama, Abdurrahman Naufal, Tadayuki Kodama, Rhythm Shimakawa, et al. Spider-Webb: Spatially-Resolved Evidence of Inside-Out Quenching in the Spiderweb Protocluster at $z \sim 2$. *arXiv e-prints*, art. arXiv:2512.18805, December 2025. doi:10.48550/arXiv.2512.18805.

[8] Novan Saputra Haryana, Masayuki Akiyama, Abdurro'uf, Hesti Retno Tri Wulandari, Juan Pablo Alfonzo, et al. Stellar mass assembly history of massive quiescent galaxies since $z \sim 4$: Insights from spatially resolved spectral energy distribution fitting with jwst data. *The Astrophysical Journal*, 994(2):215, nov 2025. doi:10.3847/1538-4357/ae03ad.

[9] A. van der Wel, M. Franx, P. G. van Dokkum, R. E. Skelton, I. G. Momcheva, et al. 3D-HST+CANDELS: The Evolution of the Galaxy Size-Mass Distribution since z = 3. *ApJ*, 788(1):28, June 2014. doi:10.1088/0004-637X/788/1/28.

[10] Caroline M. S. Straatman, Ivo Labbé, Lee R. Spitler, Karl Glazebrook, Adam Tomczak, et al. The Sizes of Massive Quiescent and Star-forming Galaxies at $z \sim 4$ with ZFOURGE and CANDELS. *ApJL*, 808(1):L29, July 2015. doi:10.1088/2041-8205/808/1/L29.

[11] Kei Ito, Francesco Valentino, Gabriel Brammer, Andreas L. Faisst, Steven Gillman, et al. Size–Stellar Mass Relation and Morphology of Quiescent Galaxies at $z \geq 3$ in Public JWST Fields. *ApJ*, 964(2):192, April 2024. doi:10.3847/1538-4357/ad2512.

[12] Z. Cemile Marsan, Danilo Marchesini, Adam Muzzin, Gabriel B. Brammer, Rachel Bezanson, et al. HST F160W Imaging of Very Massive Galaxies at $1.5 < z < 3.0$: Diversity of Structures and the Effect of Close Pairs on Number Density Estimates. *ApJ*, 871(2):201, February 2019. doi:10.3847/1538-4357/aaf808.

[13] Marco Martorano, Arjen van der Wel, Maarten Baes, Eric F. Bell, Gabriel Brammer, et al. The Size–Mass Relation at Rest-frame 1.5 μm from JWST/NIRCam in the COSMOS-WEB and PRIMER-COSMOS Fields. *ApJ*, 972(2):134, September 2024. doi:10.3847/1538-4357/ad5c6a.

[14] J. R. Weaver, O. B. Kauffmann, O. Ilbert, H. J. McCracken, A. Moneti, et al. COSMOS2020: A Panchromatic View of the Universe to $z\sim10$ from Two Complementary Catalogs. *ApJS*, 258(1):11, January 2022. doi:10.3847/1538-4365/ac3078.

[15] Masayuki Tanaka, Francesco Valentino, Sune Toft, Masato Onodera, Rhythm Shimakawa, et al. Stellar Velocity Dispersion of a Massive Quenching Galaxy at z = 4.01. *ApJL*, 885(2):L34, November 2019. doi:10.3847/2041-8213/ab4ff3.

[16] Francesco Valentino, Masayuki Tanaka, Iary Davidzon, Sune Toft, Carlos Gómez-Guijarro, et al. Quiescent Galaxies 1.5 Billion Years after the Big Bang and Their Progenitors. *ApJ*, 889(2):93, February 2020. doi:10.3847/1538-4357/ab64dc.

[17] Adam C. Carnall, Ross J. McLure, James S. Dunlop, Derek J. McLeod, Vivienne Wild, et al. A massive quiescent galaxy at redshift 4.658. *Nature*, 619(7971):716–719, July 2023. doi:10.1038/s41586-023-06158-6.

[18] Anna de Graaff, David J. Setton, Gabriel Brammer, Sam Cutler, Katherine A. Suess, et al. Efficient formation of a massive quiescent galaxy at redshift 4.9. *Nature Astronomy*, 9: 280–292, February 2025. doi:10.1038/s41550-024-02424-3.

[19] James Esdaile, Karl Glazebrook, Ivo Labbé, Edward Taylor, Corentin Schreiber, et al. Consistent Dynamical and Stellar Masses with Potential Light IMF in Massive Quiescent Galaxies at $3 < z < 4$ Using Velocity Dispersions Measurements with MOSFIRE. *ApJL*, 908(2): L35, February 2021. doi:10.3847/2041-8213/abe11e.

[20] Peter Lustig, Veronica Strazzullo, Chiara D'Eugenio, Emanuele Daddi, Maurilio Pannella, et al. Compact, bulge-dominated structures of spectroscopically confirmed quiescent galaxies at $z \simeq 3$. *MNRAS*, 501(2):2659–2676, February 2021. doi:10.1093/mnras/staa3766.

[21] Lalitwadee Kawinwanichakij, Karl Glazebrook, Themiya Nanayakkara, Glenn G. Kacprzak, Harry George Chittenden, et al. Connecting Environment, Star Formation History, and Morphology of Massive Quiescent Galaxies at $3 < z < 4$ with JWST. *ApJ*, 997(1): 29, January 2026. doi:10.3847/1538-4357/ae0a18.

[22] A. Cimatti, E. Daddi, A. Renzini, P. Cassata, E. Vanzella, et al. Old galaxies in the young Universe. *Nature*, 430(6996):184–187, July 2004. doi:10.1038/nature02668.

[23] Karl Glazebrook, Roberto G. Abraham, Patrick J. McCarthy, Sandra Savaglio, Hsiao-Wen Chen, et al. A high abundance of massive galaxies 3-6 billion years after the Big Bang. *Nature*, 430(6996):181–184, July 2004. doi:10.1038/nature02667.

[24] Piero Madau and Mark Dickinson. Cosmic Star-Formation History. *ARA&A*, 52(1):415–486, Aug 2014. doi:10.1146/annurev-astro-081811-125615.

[25] Annalisa Pillepich, Volker Springel, Dylan Nelson, Shy Genel, Jill Naiman, et al. Simulating galaxy formation with the IllustrisTNG model. *MNRAS*, 473(3):4077–4106, January 2018. doi:10.1093/mnras/stx2656.

[26] Joop Schaye, Robert A. Crain, Richard G. Bower, Michelle Furlong, Matthieu Schaller, et al. The EAGLE project: simulating the evolution and assembly of galaxies and their environments. *MNRAS*, 446(1):521–554, January 2015. doi:10.1093/mnras/stu2058.

[27] Romeel Davé, Daniel Anglés-Alcázar, Desika Narayanan, Qi Li, Mika H. Rafieferantsoa, et al. SIMBA: Cosmological simulations with black hole growth and feedback. *MNRAS*, 486(2):2827–2849, June 2019. doi:10.1093/mnras/stz937.

[28] Joop Schaye, Roi Kugel, Matthieu Schaller, John C. Helly, Joey Braspenning, et al. The FLAMINGO project: cosmological hydrodynamical simulations for large-scale structure and galaxy cluster surveys. *MNRAS*, 526(4):4978–5020, December 2023. doi:10.1093/mnras/stad2419.

[29] A. C. Carnall, D. J. McLeod, R. J. McLure, J. S. Dunlop, R. Begley, et al. A surprising abundance of massive quiescent galaxies at $3 < z < 5$ in the first data from JWST CEERS. *MNRAS*, 520(3):3974–3985, April 2023. doi:10.1093/mnras/stad369.

[30] Francesco Valentino, Gabriel Brammer, Katriona M. L. Gould, Vasily Kokorev, Seiji Fujimoto, et al. An Atlas of Color-selected Quiescent Galaxies at $z > 3$ in Public JWST Fields. *ApJ*, 947(1):20, April 2023. doi:10.3847/1538-4357/acbefa.

[31] William M. Baker, Francesco Valentino, Claudia del P. Lagos, Kei Ito, Christian Kragh Jespersen, et al. Exploring over 700 massive quiescent galaxies at $z = 2$–7: Demographics and stellar mass functions. *A&A*, 702:A270, October 2025. doi:10.1051/0004-6361/202555829.

[32] Darren J. Croton, Volker Springel, Simon D. M. White, G. De Lucia, C. S. Frenk, et al. The many lives of active galactic nuclei: cooling flows, black holes and the luminosities and colours of galaxies. *MNRAS*, 365(1):11–28, January 2006. doi:10.1111/j.1365-2966.2005.09675.x.

[33] R. G. Bower, A. J. Benson, R. Malbon, J. C. Helly, C. S. Frenk, et al. Breaking the hierarchy of galaxy formation. *MNRAS*, 370(2):645–655, August 2006. doi:10.1111/j.1365-2966.2006.10519.x.

[34] A. C. Fabian. Observational Evidence of Active Galactic Nuclei Feedback. *ARA&A*, 50:455–489, September 2012. doi:10.1146/annurev-astro-081811-125521.

[35] Minjung Park, Sirio Belli, Charlie Conroy, Benjamin D. Johnson, Rebecca L. Davies, et al. Widespread Rapid Quenching at Cosmic Noon Revealed by JWST Deep Spectroscopy. *ApJ*, 976(1):72, November 2024. doi:10.3847/1538-4357/ad7e15.

[36] Sirio Belli, Minjung Park, Rebecca L. Davies, J. Trevor Mendel, Benjamin D. Johnson, et al. Star formation shut down by multiphase gas outflow in a galaxy at a redshift of 2.45. *Nature*, 630(8015):54–58, June 2024. doi:10.1038/s41586-024-07412-1.

[37] Jan Scholtz, Francesco D'Eugenio, Roberto Maiolino, Pablo G. Pérez-González, Chiara Circosta, et al. Measurement of the gas consumption history of a massive quiescent galaxy. *Nature Astronomy*, January 2026. doi:10.1038/s41550-025-02751-z.

[38] Marie Martig, Frédéric Bournaud, Romain Teyssier, and Avishai Dekel. Morphological Quenching of Star Formation: Making Early-Type Galaxies Red. *ApJ*, 707(1):250–267, December 2009. doi:10.1088/0004-637X/707/1/250.

[39] Pieter G. van Dokkum, Marijn Franx, Mariska Kriek, Bradford Holden, Garth D. Illingworth, et al. Confirmation of the Remarkable Compactness of Massive Quiescent Galaxies at z ∼2.3: Early-Type Galaxies Did not Form in a Simple Monolithic Collapse. *ApJL*, 677(1):L5, April 2008. doi:10.1086/587874.

[40] Thorsten Naab, Peter H. Johansson, and Jeremiah P. Ostriker. Minor Mergers and the Size Evolution of Elliptical Galaxies. *ApJL*, 699(2):L178–L182, July 2009. doi:10.1088/0004-637X/699/2/L178.

[41] Ludwig Oser, Thorsten Naab, Jeremiah P. Ostriker, and Peter H. Johansson. The Cosmological Size and Velocity Dispersion Evolution of Massive Early-type Galaxies. *ApJ*, 744(1):63, January 2012. doi:10.1088/0004-637X/744/1/63.

[42] Sarah Wellons, Paul Torrey, Chung-Pei Ma, Vicente Rodriguez-Gomez, Mark Vogelsberger, et al. The formation of massive, compact galaxies at z = 2 in the Illustris simulation. *MNRAS*, 449(1):361–372, May 2015. doi:10.1093/mnras/stv303.

[43] Vicente Rodriguez-Gomez, Annalisa Pillepich, Laura V. Sales, Shy Genel, Mark Vogelsberger, et al. The stellar mass assembly of galaxies in the Illustris simulation: growth by mergers and the spatial distribution of accreted stars. *MNRAS*, 458(3):2371–2390, May 2016. doi:10.1093/mnras/stw456.

[44] Pieter G. van Dokkum, Katherine E. Whitaker, Gabriel Brammer, Marijn Franx, Mariska Kriek, et al. The Growth of Massive Galaxies Since z = 2. *ApJ*, 709(2):1018–1041, February 2010. doi:10.1088/0004-637X/709/2/1018.

[45] Sam E. Cutler, Katherine E. Whitaker, John R. Weaver, Bingjie Wang, Richard Pan, et al. Two Distinct Classes of Quiescent Galaxies at Cosmic Noon Revealed by JWST PRIMER and UNCOVER. *ApJL*, 967(2):L23, June 2024. doi:10.3847/2041-8213/ad464c.

[46] R. G. Abraham, N. R. Tanvir, B. X. Santiago, R. S. Ellis, K. Glazebrook, et al. Galaxy morphology to I=25 mag in the Hubble Deep Field. *MNRAS*, 279(3):L47–L52, April 1996. doi:10.1093/mnras/279.3.L47.

[47] Jennifer M. Lotz, Joel Primack, and Piero Madau. A New Nonparametric Approach to Galaxy Morphological Classification. *AJ*, 128(1):163–182, July 2004. doi:10.1086/421849.

[48] Bomee Lee, Mauro Giavalisco, Christina C. Williams, Yicheng Guo, Jennifer Lotz, et al. CANDELS: The Correlation between Galaxy Morphology and Star Formation Activity at z ∼2. *ApJ*, 774(1):47, September 2013. doi:10.1088/0004-637X/774/1/47.

[49] Yao Yao, Jie Song, Xu Kong, Guanwen Fang, Hong-Xin Zhang, et al. Evolution of Non-parametric Morphology of Galaxies in the JWST CEERS Field at z ≃ 0.8-3.0. *ApJ*, 954(2):113, September 2023. doi:10.3847/1538-4357/ace7b5.

[50] Jeyhan S. Kartaltepe, Caitlin Rose, Brittany N. Vanderhoof, Elizabeth J. McGrath, Luca

Costantin, et al. CEERS Key Paper. III. The Diversity of Galaxy Structure and Morphology at z = 3-9 with JWST. *ApJL*, 946(1):L15, March 2023. doi:10.3847/2041-8213/acad01.

[51] S. Tacchella, C. M. Carollo, A. Renzini, N. M. Förster Schreiber, P. Lang, et al. Evidence for mature bulges and an inside-out quenching phase 3 billion years after the Big Bang. *Science*, 348(6232):314–317, April 2015. doi:10.1126/science.1261094.

[52] Justin S. Spilker, Rachel Bezanson, Benjamin J. Weiner, Katherine E. Whitaker, and Christina C. Williams. Evidence for Inside-out Galaxy Growth and Quenching of a z $\sim$ 2 Compact Galaxy From High-resolution Molecular Gas Imaging. *ApJ*, 883(1):81, September 2019. doi:10.3847/1538-4357/ab3804.

[53] R. M. González Delgado, R. Cid Fernandes, E. Pérez, R. García-Benito, R. López Fernández, et al. Star formation along the Hubble sequence. Radial structure of the star formation of CALIFA galaxies. *A&A*, 590:A44, May 2016. doi:10.1051/0004-6361/201628174.

[54] Lihwai Lin, Bau-Ching Hsieh, Hsi-An Pan, Sandro B. Rembold, Sebastián F. Sánchez, et al. SDSS-IV MaNGA: Inside-out versus Outside-in Quenching of Galaxies in Different Local Environments. *ApJ*, 872(1):50, February 2019. doi:10.3847/1538-4357/aafa84.

[55] Erica J. Nelson, Sandro Tacchella, Benedikt Diemer, Joel Leja, Lars Hernquist, et al. Spatially resolved star formation and inside-out quenching in the TNG50 simulation and 3D-HST observations. *MNRAS*, 508(1):219–235, November 2021. doi:10.1093/mnras/stab2131.

[56] Charlie Conroy. Modeling the Panchromatic Spectral Energy Distributions of Galaxies. *ARA&A*, 51(1):393–455, August 2013. doi:10.1146/annurev-astro-082812-141017.

[57] Kartheik G. Iyer, Camilla Pacifici, Gabriela Calistro-Rivera, and Christopher C. Lovell. The Spectral Energy Distributions of Galaxies. *arXiv e-prints*, art. arXiv:2502.17680, February 2025. doi:10.48550/arXiv.2502.17680.

[58] Rachel Bezanson, Ivo Labbe, Katherine E. Whitaker, Joel Leja, Sedona H. Price, et al. The JWST UNCOVER Treasury Survey: Ultradeep NIRSpec and NIRCam Observations before

the Epoch of Reionization. *ApJ*, 974(1):92, October 2024. doi:10.3847/1538-4357/ad66cf.

[59] Katherine A. Suess, John R. Weaver, Sedona H. Price, Richard Pan, Bingjie Wang, et al. Medium Bands, Mega Science: A JWST/NIRCam Medium-band Imaging Survey of A2744. *ApJ*, 976(1):101, November 2024. doi:10.3847/1538-4357/ad75fe.

[60] A C Carnall, R J McLure, J S Dunlop, and R Davé. Inferring the star formation histories of massive quiescent galaxies with bagpipes: evidence for multiple quenching mechanisms. *Monthly Notices of the Royal Astronomical Society*, 480(4):4379–4401, 08 2018. ISSN 0035-8711. doi:10.1093/mnras/sty2169.

[61] Vicente Rodriguez-Gomez, Gregory F. Snyder, Jennifer M. Lotz, Dylan Nelson, Annalisa Pillepich, et al. The optical morphologies of galaxies in the IllustrisTNG simulation: a comparison to Pan-STARRS observations. *Monthly Notices of the Royal Astronomical Society*, 483(3):4140–4159, March 2019. doi:10.1093/mnras/sty3345.

[62] Imad Pasha and Tim B. Miller. pysersic: A python package for determining galaxy structural properties via bayesian inference, accelerated with jax. *Journal of Open Source Software*, 8 (89):5703, 2023. doi:10.21105/joss.05703.

[63] Abdurro'uf, Yen-Ting Lin, Po-Feng Wu, and Masayuki Akiyama. Introducing piXedfit: A Spectral Energy Distribution Fitting Code Designed for Resolved Sources. *ApJS*, 254(1): 15, May 2021. doi:10.3847/1538-4365/abebe2.

[64] Nicholas S. Martis, Sunna Withers, Maruša Bradač, Adam Muzzin, Giordano Felicioni, et al. CANUCS/Technicolor: JWST Medium-band Photometry Finds Half of the Star Formation at z > 7.5 Is Obscured. *ApJ*, 990(1):83, September 2025. doi:10.3847/1538-4357/adf32a.

[65] Planck Collaboration, N. Aghanim, Y. Akrami, M. Ashdown, J. Aumont, et al. Planck 2018 results. VI. Cosmological parameters. *A&A*, 641:A6, September 2020. doi:10.1051/0004-6361/201833910.

[66] Sedona H. Price, Rachel Bezanson, Ivo Labbe, Lukas J. Furtak, Anna de Graaff, et al. The UNCOVER Survey: First Release of Ultradeep JWST/NIRSpec PRISM Spectra for $\sim$700 Galaxies from z $\sim$ 0.3–13 in A2744. *ApJ*, 982(1):51, March 2025. doi:10.3847/1538-4357/adaec1.

[67] John R. Weaver, Sam E. Cutler, Richard Pan, Katherine E. Whitaker, Ivo Labbé, et al. The UNCOVER Survey: A First-look HST + JWST Catalog of 60,000 Galaxies near A2744 and beyond. *ApJS*, 270(1):7, January 2024. doi:10.3847/1538-4365/ad07e0.

[68] T. Treu, G. Roberts-Borsani, M. Bradac, G. Brammer, A. Fontana, et al. The GLASS-JWST Early Release Science Program. I. Survey Design and Release Plans. *ApJ*, 935(2): 110, August 2022. doi:10.3847/1538-4357/ac8158.

[69] Rohan P. Naidu, Jorryt Matthee, Ivan Kramarenko, Andrea Weibel, Gabriel Brammer, et al. All the Little Things in Abell 2744: $>$1000 Gravitationally Lensed Dwarf Galaxies at $z = 0-9$ from JWST NIRCam Grism Spectroscopy. *arXiv e-prints*, art. arXiv:2410.01874, October 2024. doi:10.48550/arXiv.2410.01874.

[70] Gabe Brammer. Grizli: Grism redshift and line analysis software, May 2019.

[71] Gabe Brammer and Jasleen Matharu. gbrammer/grizli: Release 2021, June 2021.

[72] Gabriel Brammer. msaexp: Nirspec analyis tools, September 2023.

[73] Anna de Graaff, Hans-Walter Rix, Stefano Carniani, Katherine A. Suess, Stéphane Charlot, et al. Ionised gas kinematics and dynamical masses of z $\gtrsim$ 6 galaxies from JADES/NIRSpec high-resolution spectroscopy. *A&A*, 684:A87, April 2024. doi:10.1051/0004-6361/202347755.

[74] Kasper E. Heintz, Darach Watson, Gabriel Brammer, Simone Vejlgaard, Anne Hutter, et al. Strong damped Lyman-α absorption in young star-forming galaxies at redshifts 9 to 11. *Science*, 384(6698):890–894, May 2024. doi:10.1126/science.adj0343.

[75] G. Bruzual and S. Charlot. Stellar population synthesis at the resolution of 2003. *Monthly Notices of the Royal Astronomical Society*, 344(4):1000–1028, 10 2003. ISSN 0035-8711. doi:10.1046/j.1365-8711.2003.06897.x.

[76] P. Kroupa and C. M. Boily. On the mass function of star clusters. *Monthly Notices of the Royal Astronomical Society*, 336(4):1188–1194, 11 2002. ISSN 0035-8711. doi:10.1046/j.1365-8711.2002.05848.x.

[77] F. Feroz and M. P. Hobson. Multimodal nested sampling: an efficient and robust alternative to Markov Chain Monte Carlo methods for astronomical data analyses. *MNRAS*, 384(2): 449–463, February 2008. doi:10.1111/j.1365-2966.2007.12353.x.

[78] F. Feroz, M. P. Hobson, and M. Bridges. MULTINEST: an efficient and robust Bayesian inference tool for cosmology and particle physics. *MNRAS*, 398(4):1601–1614, October 2009. doi:10.1111/j.1365-2966.2009.14548.x.

[79] Farhan Feroz, Michael P. Hobson, Ewan Cameron, and Anthony N. Pettitt. Importance Nested Sampling and the MultiNest Algorithm. *The Open Journal of Astrophysics*, 2(1):10, November 2019. doi:10.21105/astro.1306.2144.

[80] J. Buchner, A. Georgakakis, K. Nandra, L. Hsu, C. Rangel, et al. X-ray spectral modelling of the AGN obscuring region in the CDFS: Bayesian model selection and catalogue. *Astronomy & Astrophysics*, 564:A125, 2014. doi:10.1051/0004-6361/201322971.

[81] Benjamin D. Johnson. bd-j/sedpy: sedpy v0.2.0, March 2021.

[82] M. Franx, P. G. van Dokkum, N. M. Förster Schreiber, S. Wuyts, I. Labbé, et al. Structure and Star Formation in Galaxies out to z = 3: Evidence for Surface Density Dependent Evolution and Upsizing. *The Astrophysical Journal*, 688:770–788, 2008. doi:10.1086/592431.

[83] A. Gallazzi, E. F. Bell, S. Zibetti, J. Brinchmann, and D. D. Kelson. Charting the Evolution of the Ages and Metallicities of Massive Galaxies since z = 0.7. *The Astrophysical Journal*, 788(1):72, 2014. doi:10.1088/0004-637X/788/1/72.

[84] Corentin Schreiber, Karl Glazebrook, Themiya Nanayakkara, Glenn G. Kacprzak, Pascal A. Oesch, et al. Near-infrared spectroscopy of $0.4 < z < 1.0$ FMOS-COSMOS emission-line galaxies. *Astronomy & Astrophysics*, 618:A85, 2018. doi:10.1051/0004-6361/201833070.

[85] Jared C. Siegel, Rachel Bezanson, Gourav Khullar, Sedona H. Price, David J. Setton, et al. UNCOVER: Significant Reddening in Cosmic Noon Quiescent Galaxies. *The Astrophysical Journal*, 977(2):249, 2025. doi:10.3847/1538-4357/adc7b7.

[86] Jose Luis Sersic. *Atlas de Galaxias Australes*. 1968.

[87] Larry Bradley, Brigitta Sipőcz, Thomas Robitaille, Erik Tollerud, Zé Vinícius, et al. astropy/photutils: 2.3.0, September 2025.

[88] Nicola De Cao, Ivan Titov, and Wilker Aziz. Block neural autoregressive flow, 2019. URL https://arxiv.org/abs/1904.04676.

[89] E. Bertin and S. Arnouts. SExtractor: Software for source extraction. *A&AS*, 117:393–404, June 1996. doi:10.1051/aas:1996164.

[90] Kyle Barbary. Sep: Source extractor as a library. *Journal of Open Source Software*, 1(6): 58, 2016. doi:10.21105/joss.00058.

[91] Michele Cappellari and Yannick Copin. Adaptive spatial binning of integral-field spectroscopic data using voronoi tessellations. *Monthly Notices of the Royal Astronomical Society*, 342(2):345–354, 06 2003. ISSN 0035-8711. doi:10.1046/j.1365-8711.2003.06541.x.

[92] Abdurro'uf and Masayuki Akiyama. Understanding the scatter in the spatially resolved star formation main sequence of local massive spiral galaxies. *Monthly Notices of the Royal Astronomical Society*, 469(3):2806–2820, 05 2017. ISSN 0035-8711. doi:10.1093/mnras/stx936.

[93] Charlie Conroy, James E. Gunn, and Martin White. The propagation of uncertainties in stellar population synthesis modeling. i. the relevance of uncertain aspects of stellar evolution and the initial mass function to the derived physical properties of galaxies. *The Astrophysical Journal*, 699(1):486, 06 2009. doi:10.1088/0004-637X/699/1/486.

[94] Charlie Conroy and James E. Gunn. The propagation of uncertainties in stellar population synthesis modeling. iii. model calibration, comparison, and evaluation. *The Astrophysical Journal*, 712(2):833, 03 2010. doi:10.1088/0004-637X/712/2/833.

[95] Dan Foreman-Mackey, Jonathan Sick, and Ben Johnson. python-fsps: Python bindings to fsps (v0.1.1), October 2014.

[96] L. Girardi, A. Bressan, G. Bertelli, and C. Chiosi. Evolutionary tracks and isochrones for low- and intermediate-mass stars: From 0.15 to 7 M_{sun}, and from Z=0.0004 to 0.03. *A&AS*, 141:371–383, February 2000. doi:10.1051/aas:2000126.

[97] P. Marigo and L. Girardi. Evolution of asymptotic giant branch stars. I. Updated synthetic TP-AGB models and their basic calibration. *A&A*, 469(1):239–263, July 2007. doi:10.1051/0004-6361:20066772.

[98] P. Marigo, L. Girardi, A. Bressan, M. A. T. Groenewegen, L. Silva, et al. Evolution of asymptotic giant branch stars. II. Optical to far-infrared isochrones with improved TP-AGB models. *A&A*, 482(3):883–905, May 2008. doi:10.1051/0004-6361:20078467.

[99] P. Sánchez-Blázquez, R. F. Peletier, J. Jiménez-Vicente, N. Cardiel, A. J. Cenarro, et al. Medium-resolution Isaac Newton Telescope library of empirical spectra. *MNRAS*, 371(2):703–718, September 2006. doi:10.1111/j.1365-2966.2006.10699.x.

[100] J. Falcón-Barroso, P. Sánchez-Blázquez, A. Vazdekis, E. Ricciardelli, N. Cardiel, et al. An updated MILES stellar library and stellar population models. *A&A*, 532:A95, August 2011. doi:10.1051/0004-6361/201116842.

[101] D. Calzetti, L. Armus, R. C. Bohlin, A. L. Kinney, J. Koornneef, et al. The Dust Content and Opacity of Actively Star-forming Galaxies. *The Astrophysical Journal*, 533(2):682–695, 2000. doi:10.1086/308692.

[102] B. T. Draine and Aigen Li. Infrared Emission from Interstellar Dust. IV. The Silicate-Graphite-PAH Model in the Post-Spitzer Era. *ApJ*, 657(2):810–837, March 2007. doi:10.1086/511055.

[103] Nell Byler, Julianne J. Dalcanton, Charlie Conroy, and Benjamin D. Johnson. Nebular Continuum and Line Emission in Stellar Population Synthesis Models. *ApJ*, 840(1):44, May 2017. doi:10.3847/1538-4357/aa6c66.

[104] G. J. Ferland, K. T. Korista, D. A. Verner, J. W. Ferguson, J. B. Kingdon, et al. CLOUDY 90: Numerical Simulation of Plasmas and Their Spectra. *PASP*, 110(749):761–778, July 1998. doi:10.1086/316190.

[105] G. J. Ferland, R. L. Porter, P. A. M. van Hoof, R. J. R. Williams, N. P. Abel, et al. The 2013 Release of Cloudy. *Rev. Mex. Astron. Astrofis.*, 49:137–163, April 2013. doi:10.48550/arXiv.1302.4485.

[106] J. Maíz Apellániz. A Recalibration of Optical Photometry: Tycho-2, Strömgren, and Johnson Systems. *AJ*, 131(2):1184–1199, February 2006. doi:10.1086/499158.

[107] M. F. Skrutskie, R. M. Cutri, R. Stiening, M. D. Weinberg, S. Schneider, et al. The Two Micron All Sky Survey (2MASS). *AJ*, 131(2):1163–1183, February 2006. doi:10.1086/498708.

[108] Omkar Bait, Sudhanshu Barway, and Yogesh Wadadekar. On the interdependence of galaxy morphology, star formation and environment in massive galaxies in the nearby Universe. *MNRAS*, 471(3):2687–2702, November 2017. doi:10.1093/mnras/stx1688.

[109] Philip F. Hopkins, Dušan Kereš, José Oñorbe, Claude-André Faucher-Giguère, Eliot Quataert, et al. Galaxies on FIRE (Feedback In Realistic Environments): stellar feedback explains cosmologically inefficient star formation. *MNRAS*, 445(1):581–603, November 2014. doi:10.1093/mnras/stu1738.

[110] Katherine E. Whitaker, Marijn Franx, Rachel Bezanson, Gabriel B. Brammer, Pieter G. van Dokkum, et al. Galaxy Structure as a Driver of the Star Formation Sequence Slope and Scatter. *ApJL*, 811(1):L12, September 2015. doi:10.1088/2041-8205/811/1/L12.

[111] Hsi-An Pan, Lihwai Lin, Bau-Ching Hsieh, Sebastián F. Sánchez, Héctor Ibarra-Medel, et al. SDSS IV MaNGA: Dependence of Global and Spatially Resolved SFR-M $_*$ Relations on Galaxy Properties. *ApJ*, 854(2):159, February 2018. doi:10.3847/1538-4357/aaa9bc.

[112] R. M. González Delgado, R. García-Benito, E. Pérez, R. Cid Fernandes, A. L. de Amorim, et al. The CALIFA survey across the Hubble sequence. Spatially resolved stellar popula-

tion properties in galaxies. *A&A*, 581:A103, September 2015. doi:10.1051/0004-6361/201525938.

[113] Richard M. McDermid, Katherine Alatalo, Leo Blitz, Frédéric Bournaud, Martin Bureau, et al. The ATLAS^{3D} Project - XXX. Star formation histories and stellar population scaling relations of early-type galaxies. *MNRAS*, 448(4):3484–3513, April 2015. doi:10.1093/mnras/stv105.

[114] R. López Fernández, R. M. González Delgado, E. Pérez, R. García-Benito, R. Cid Fernandes, et al. Cosmic evolution of the spatially resolved star formation rate and stellar mass of the CALIFA survey. *A&A*, 615:A27, July 2018. doi:10.1051/0004-6361/201732358.

[115] Philip F. Hopkins, Lars Hernquist, Thomas J. Cox, and Dušan Kereš. A Cosmological Framework for the Co-Evolution of Quasars, Supermassive Black Holes, and Elliptical Galaxies. I. Galaxy Mergers and Quasar Activity. *ApJS*, 175(2):356–389, April 2008. doi:10.1086/524362.

[116] Rachel S. Somerville, Philip F. Hopkins, Thomas J. Cox, Brant E. Robertson, and Lars Hernquist. A semi-analytic model for the co-evolution of galaxies, black holes and active galactic nuclei. *MNRAS*, 391(2):481–506, December 2008. doi:10.1111/j.1365-2966.2008.13805.x.

[117] Rainer Weinberger, Volker Springel, Lars Hernquist, Annalisa Pillepich, Federico Marinacci, et al. Simulating galaxy formation with black hole driven thermal and kinetic feedback. *MNRAS*, 465(3):3291–3308, March 2017. doi:10.1093/mnras/stw2944.

[118] Yohan Dubois, Sébastien Peirani, Christophe Pichon, Julien Devriendt, Raphaël Gavazzi, et al. The HORIZON-AGN simulation: morphological diversity of galaxies promoted by AGN feedback. *MNRAS*, 463(4):3948–3964, December 2016. doi:10.1093/mnras/stw2265.

[119] Rainer Weinberger, Volker Springel, Rüdiger Pakmor, Dylan Nelson, Shy Genel, et al. Supermassive black holes and their feedback effects in the IllustrisTNG simulation. *MNRAS*, 479(3):4056–4072, September 2018. doi:10.1093/mnras/sty1733.